

# A Global 3-D Simulation of Magnetospheric Accretion: I. Magnetically Disrupted Discs and Surface Accretion

ZHAOHUAN ZHU,<sup>1,2</sup> JAMES M. STONE,<sup>3</sup> AND NURIA CALVET<sup>4</sup>

<sup>1</sup>*Department of Physics and Astronomy, University of Nevada, Las Vegas, 4505 S. Maryland Pkwy, Las Vegas, NV, 89154, USA*

<sup>2</sup>*Nevada Center for Astrophysics, University of Nevada, Las Vegas, 4505 S. Maryland Pkwy, Las Vegas, NV, 89154, USA*

<sup>3</sup>*Institute for Advanced Study, 1 Einstein Drive, Princeton, NJ, 08540, USA*

<sup>4</sup>*Department of Astronomy, University of Michigan, 1085 South University Ave., Ann Arbor, MI 48109, USA*

## ABSTRACT

We present a 3-D ideal MHD simulation of magnetospheric accretion onto a non-rotating star. The accretion process unfolds with intricate 3-D structures driven by various mechanisms. First, the disc develops filaments at the magnetospheric truncation radius ( $R_T$ ) due to magnetic interchange instability. These filaments penetrate deep into the magnetosphere, form multiple accretion columns, and eventually impact the star at  $\sim 30^\circ$  from the poles at nearly the free-fall speed. Over 50% (90%) of accretion occurs on just 5% (20%) of the stellar surface. Second, the disc region outside  $R_T$  develops large-scale magnetically dominated bubbles, again due to magnetic interchange instability. These bubbles orbit at a sub-Keplerian speed, persisting for a few orbits while leading to asymmetric mass ejection. The disc outflow is overall weak because of mostly closed field lines. Third, magnetically-supported surface accretion regions appear above the disc, resembling a magnetized disc threaded by net vertical fields, a departure from traditional magnetospheric accretion models. Stellar fields are efficiently transported into the disc region due to above instabilities, contrasting with the “X-wind” model. The accretion rate onto the star remains relatively steady with a 23% standard deviation. The periodogram reveals variability occurring at around 0.2 times the Keplerian frequency at  $R_T$ , linked to the large-scale magnetic bubbles. The ratio of the spin-up torque to  $\dot{M}(GM_*R_T)^{1/2}$  is around 0.8. Finally, after scaling the simulation, we investigate planet migration in the inner protoplanetary disc. The disc driven migration is slow in the MHD turbulent disc beyond  $R_T$ , while aerodynamic drag plays a significant role in migration within  $R_T$ .

*Keywords:* accretion, accretion discs - dynamo - magnetohydrodynamics (MHD) - instabilities - X-rays: binaries - protoplanetary discs

## 1. INTRODUCTION

Magnetospheric accretion plays a key role in many astrophysical systems, from neutron stars (e.g. Lewin & van der Klis 2006) to T-Tauri stars (Hartmann et al. 2016) and even young planets (Wagner et al. 2018; Haffert et al. 2019; Zhou et al. 2021)<sup>1</sup>. For neutron stars, it could be related to the spin-up/spin-down of accreting X-ray pulsars (Bildsten et al. 1997), QPOs in low-mass X-ray binaries (van der Klis 2006), ultraluminous X-ray sources (King et al. 2023), and relativistic jets/outflows (Fender et al. 2004), the latter of which are crucial for studying Gamma-ray bursts and neutron star mergers. For T-Tauri stars, magnetospheric accretion is di-

rectly detected via accretion shocks at the surface of the star (Calvet & Gullbring 1998; Ingleby et al. 2011) and atomic lines produced within the magnetosphere (Hartmann et al. 1994; Muzerolle et al. 1998, 2001), which serve as the main ways to constrain the disc accretion rates (Rigliaco et al. 2012; Manara et al. 2013; Espaillat et al. 2022). Magnetospheric accretion also affects the structure of protoplanetary discs within 1 au, which is crucial for studying the formation of close-in exoplanets (Lee & Chiang 2017; Liu et al. 2017). For young planets, magnetospheric accretion may be responsible for the detected  $H_\alpha$  lines around young giant planets (e.g. Zhu 2015; Thanathibodee et al. 2019a; Marleau et al. 2022, but see Aoyama et al. 2018; Szulágyi & Ercolano 2020), and emission from magnetospheric accretion could reveal young planets in protoplanetary discs.

Magnetospheric accretion is a complex process primarily driven by the influence of the stellar magnetic fields. The magnetic field strength decreases sharply as distance from the star increases. In close proximity to the star, stellar fields are so strong that the flow is in

Corresponding author: Zhaohuan Zhu  
zhaohuan.zhu@unlv.edu

<sup>1</sup> The problem generator and input file for the simulation presented in this work can be found at <https://github.com/zhuzh1983/magnetospheric2023>

the force-free regime. Moving outwards to the magnetospheric truncation radius, the flow and magnetic fields are dynamically balanced and the flow is in the strong field regime. Further out into the disc, the disc thermal pressure is far higher than the magnetic pressure so that the disc enters the weak field regime, where disc instabilities (e.g. magneto-rotational instability, MRI) could play an essential role in disc accretion.

Several outstanding theoretical questions persist regarding magnetospheric accretion, as reviewed by [Lai 2014](#): 1) how do the stellar magnetic fields connect with the disc? 2) Can accretion occur steadily throughout the region? 3) What controls the stellar spin? 4) How are outflows launched? and many others. To address these questions, numerous models have been proposed. In a seminal paper, [Ghosh & Lamb \(1979a\)](#) supposed that stellar fields can permeate a substantial radial region of the disc, reaching a steady state when field dragging is balanced by dissipation. This model suggests the existence of a broad transition zone (a detailed description of this model is given in §2.1). However, alternative models propose that the disc is a good conductor so that the field lines are pinched inwards at the boundary ([Arons & Barnard 1986](#), "X-wind" model from [Shu et al. 1994](#)). Furthermore, some models suggest that the accretion is not steady (e.g. [Aly & Kijpers 1990](#); [Lovelace et al. 1995](#); [Uzdensky et al. 2002](#)). In these scenarios, magnetic fields connecting the star and the disc undergo winding, causing the flux tube to expand with building magnetic pressure - so called "field inflation". Subsequently, reconnection events take place, leading to the expulsion of outer field lines, resulting in mass ejection. Meanwhile, the inner reconnected field lines continue to wind up, perpetuating this cyclic process.

Magnetospheric accretion could also be linked to the launching of jets and winds, expanding the scope beyond the conventional extended disc winds ([Blandford & Payne 1982](#); [Wardle & Koenigl 1993](#); [Ferreira & Pelletier 1995](#); [Casse & Ferreira 2000](#)) and stellar winds ([Sauty & Tsinganos 1994](#); [Hartmann & MacGregor 1980](#)). Various models have been suggested, including accretion-powered stellar winds ([Matt & Pudritz 2005](#)), a wide-angle "X-wind" ([Shu et al. 1994](#)), or even unsteady magnetospheric winds due to reconnection ([Ferreira et al. 2000](#); [Hayashi et al. 1996](#); [Matt et al. 2002](#)).

More detailed insights have been unveiled through direct numerical simulations (see review by [Romanova & Owocki 2015](#)). Earlier simulations employed axisymmetric 2-D configurations ([Goodson et al. 1997](#); [Miller & Stone 1997](#); [Fendt & Elstner 2000](#)). These simulations have already revealed that the accretion structure depends sensitively on the initial stellar and disc field configurations (e.g. parallel or anti-parallel). Both accretion and stellar winds ([Zanni & Ferreira 2013](#)) could also vary strongly with time in these simulations. Later, 3-D simulations have been carried out ([Romanova et al. 2003b, 2004b](#)). Given the difficulty in simulating the

polar region using the conventional spherical-polar coordinate system in 3-D, [Romanova et al. \(2003b\)](#) adopt the "cubed sphere" grid. To simulate the accretion disc, an  $\alpha$  viscosity is adopted in the disc region. Tilted dipole fields ([Romanova et al. 2003b](#)), fast rotators ([Romanova et al. 2004a](#)), tilted rotating stars with tilted dipole fields ([Romanova et al. 2020](#)) have all been studied. These works show that the accretion structure depends on the dipole tilt angle. Furthermore, warping of the disc, interchange instability, and Rayleigh-Taylor instability ([Kulkarni & Romanova 2008](#)) can all play important roles for accretion with tilted dipole fields. However, due to the use of an  $\alpha$  viscosity, the self-consistent treatment of disc accretion driven by the MRI is not achieved in these models.

MHD simulations including both the magnetosphere and MRI turbulence have been carried out with both axisymmetric 2-D and fully 3-D simulations ([Romanova et al. 2011, 2012](#)). The 3-D simulations again use the "cubed sphere" configuration. Both boundary layer accretion with weak fields and magnetospheric accretion with strong fields have been explored. These simulations reveal significant accretion variability. They show that the stress in the accretion disc is consistent with local MRI simulations. On the other hand, the global flow structure has not been thoroughly examined.

Recent global MHD simulations reveal that, for discs threaded by external vertical magnetic fields (without including the stellar fields), the flow structure is dramatically different from that in local MRI simulations. The disc accretion structure sensitively depends on the strength of net vertical magnetic fields. When the net field is relatively weak (initial plasma  $\beta \sim 10^3 - 10^4$  at the disc midplane), most accretion occurs in the magnetically supported disc surface region that can extend vertically to  $z \sim R$  ([Beckwith et al. 2009](#); [Zhu & Stone 2018](#); [Takasao et al. 2018](#); [Mishra et al. 2020](#); [Jacquemin-Idre et al. 2021](#)). A quasi-static global field geometry is established when the flux transport by the fast inflow at the surface is balanced by the slow vertical turbulent diffusion. When strong vertical fields thread the disc around black-holes (BH), the disc flow can enter the regime of magnetically arrested discs (MAD, [Narayan et al. 2003](#); [Igumenshchev et al. 2003](#)), where the accumulated poloidal fields disrupt the accretion flow to become discrete blobs/streams and the blobs/streams fight their way towards the BH through magnetic interchanges and reconnections. With poloidal magnetic fields acting like a wire lowering material down to the BH, the MAD state leads to the efficient release of the rest mass energy and strong quasi-periodic outflows ([Tchekhovskoy et al. 2011](#)). The variability may be related to low-frequency QPOs, variability in AGN, and GRB outflows ([Proga & Zhang 2006](#)). Considering that the disc-threading stellar dipole fields weaken sharply with distance to the star (from force-free, strong fields, to weak fields), some aspects of the MAD state and the

newly discovered surface accretion mode can be applied to magnetospheric accretion.

Furthermore, owing to the high computational cost in 3-D simulations, most previous 3-D magnetospheric accretion simulations cannot follow the disc evolution over the viscous timescale, and thus focused on studying the magnetosphere itself. However, magnetospheric accretion plays a pivotal role in shaping the disc's long-term evolution. An unresolved challenge within accretion disc theory is the uncertainty of the inner boundary conditions, except for accretion onto black holes. For example, zero torque or zero mass flux inner conditions lead to different disc evolution paths (Lynden-Bell & Pringle 1974). The proper inner boundary condition can only be understood if we incorporate the central object in the disc simulation. To study the interplay between the magnetosphere and the disc, encompassing all three different MHD regimes, we carry out high-resolution long-timescale global simulations that incorporate both the magnetized star and the disc. As a first step, we adopt the simplest setup which only includes a non-rotating star with a dipole field surrounded by an accretion disc. The disc is threaded by the stellar field only (without the external field) to avoid the complex interaction between the stellar and external fields. Since the star is non-rotating, the corotation radius is at infinity. Such a simple setup allows us to model a relatively clean problem as the foundation for future more realistic simulations. Nevertheless, this setup can be directly applied to slow rotators in many astrophysical systems. On the other hand, this setup does not allow us to study accretion around fast rotators, which could launch powerful jets and winds (Miller & Stone 1997; Lovelace et al. 1999; Romanova et al. 2018) that make the star to spin down (Matt & Pudritz 2005). While we were preparing this manuscript, Takasao et al. (2022) published the results of 3-D ideal MHD simulations studying magnetospheric accretion onto stars with different spin rates. Our work and Takasao et al. (2022) share some similarities, but also bear significant differences. By exploring stars with different spin rates, Takasao et al. (2022) can address how wind launching and spin-up/down torque is affected by the stellar spin. On the other hand, our simulation adopts a Cartesian grid with mesh-refinement, which significantly reduces the computational cost. This allows our simulation to include a relatively large magnetosphere generated from the 1kG stellar dipole (compared with 100 G in Takasao et al. 2022) and study the disc evolution on much longer timescales (2000 vs 400 innermost orbits). Thus, besides the processes within the magnetosphere, we can study the dynamics of the disc over a large dynamical range and explore how the disc and the magnetosphere interact with each other in a quasi-steady accretion stage.

In §2, we lay out the theoretical framework for magnetospheric accretion, and introduce the key physical quantities in the classical Ghosh & Lamb (1979a) model.

Our numerical model is presented in §3. We present results in §4 from the inner magnetosphere to the outer disc. After discussions in §5, we conclude the paper in §6.

## 2. THEORETICAL FRAMEWORK

### 2.1. The Classical Model

The magnetospheric accretion model by Ghosh & Lamb (1979a) is summarized in the left panel of Figure 1. In close proximity to the star, magnetic fields are so strong that the plasma is forced to corotate with the star. For an axisymmetric and steady flow, the plasma structure there can be solved via four conserved quantities which are constant along magnetic field lines (Ghosh et al. 1977). These four constants (Mestel 1961; Weber & Davis 1967) are also widely used in disc wind studies (Blandford & Payne 1982). When  $\mathbf{v}$  and  $\mathbf{B}$  are separated into the poloidal and toroidal components ( $\mathbf{v} = \mathbf{v}_p + \Omega R \mathbf{e}_\phi$  and  $\mathbf{B} = \mathbf{B}_p + B_\phi \mathbf{e}_\phi$ ), the induction equation implies that  $\mathbf{v}_p$  and  $\mathbf{B}_p$  are in the same direction, and the first constant is

$$k = \frac{\rho \mathbf{v}_p}{\mathbf{B}_p}, \quad (1)$$

which is the mass loading parameter. In the azimuthal direction, we have the second constant

$$\omega_s = \Omega - \frac{k B_\phi}{\rho R}. \quad (2)$$

Note that  $\omega_s$  should be equal to the angular frequency of the star, denoted as  $\Omega_s$ . Otherwise, there is a strong shear at the stellar surface where  $v_p$  decreases to 0. Equations 1 and 2 imply that, in the rotating frame with the angular frequency  $\omega_s$ , the flow's velocity is in the same direction as the magnetic field lines, or in simpler terms, the material flows along the field lines. We can define the pitch angle of the magnetic field lines as  $\psi \equiv B_p/B_\phi$ . Using the angular momentum equation, we have the third constant

$$l = R(v_\phi - \frac{B_\phi}{k}), \quad (3)$$

which is the specific angular momentum of the flow. In a barotropic fluid, Bernoulli's equation can be used to derive the fourth constant

$$\begin{aligned} e &= \frac{1}{2}v^2 + \Phi + h + \frac{B^2}{\rho} - \frac{\mathbf{B} \cdot \mathbf{v}}{k} \\ &= \frac{1}{2}v^2 + \Phi + h + \frac{B_\phi B_p}{\rho} - \frac{B_\phi v_\phi}{k}, \end{aligned} \quad (4)$$

where  $h$  is  $\int_0^p dp/\rho$ . For a strongly magnetized plasma,  $h$  is much smaller than other terms. Within the magnetosphere, the poloidal velocity and gravitational term dominate in Equation 4, so that the poloidal velocity

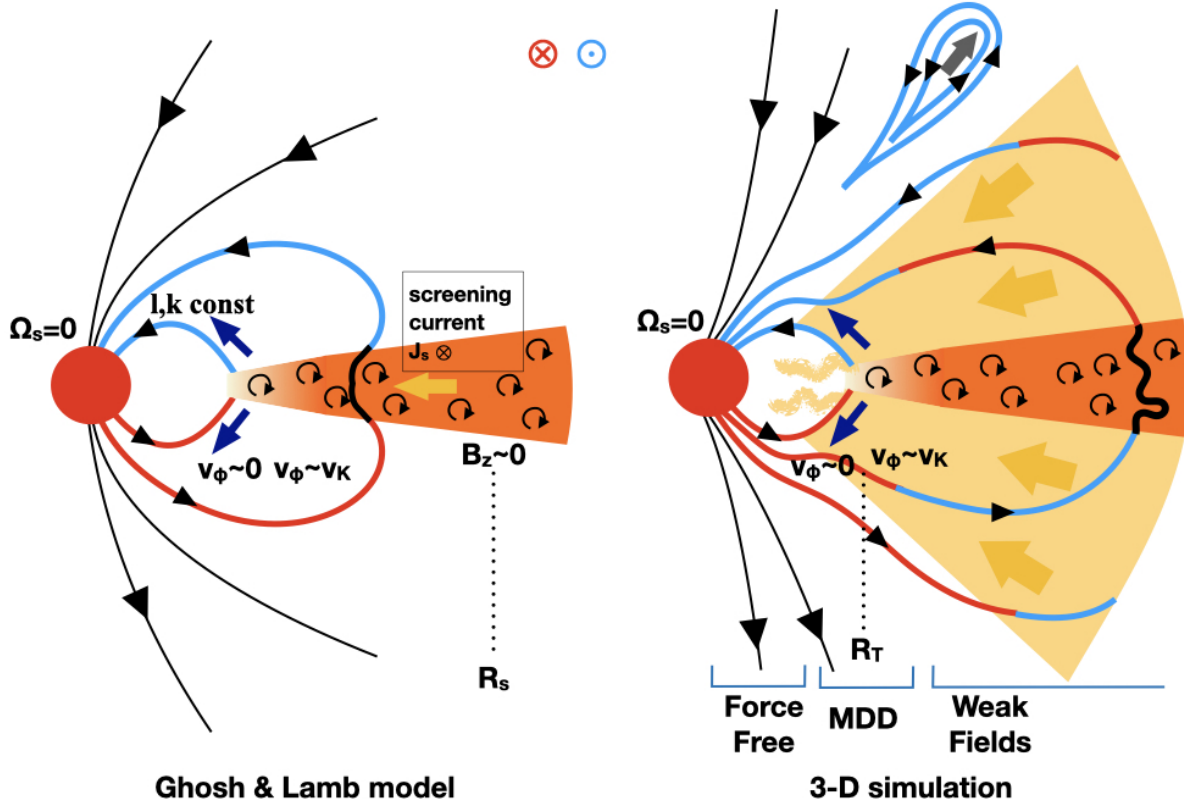


**Figure 1.** The flow and magnetic field structure in the magnetospheric accretion model of Ghosh & Lamb (1979a) (the left panel) and in our 3-D simulations (the right panel). The solid curves represent the magnetic field lines. The red and blue colors represent  $B$  fields with positive and negative  $B_\phi$  components. The yellow and purple arrows label the flow with positive and negative  $v_\phi$  components respectively. The positive  $\phi$  component indicates the same direction as disc rotation. The screening current in the traditional model has a positive  $\phi$  component, which leads to the vanishing stellar  $B_z$  beyond  $R_s$ .  $R_s$  is the screening radius where  $B_z = 0$ . The most noticeable difference between the two models include the highly magnetized surface layer which inflows at supersonic speeds. Keplerian shear in this layer drags the radial magnetic field lines to develop significant  $B_\phi$  components inside the layer. Other differences include the filaments and density voids in the magnetically disrupted disc (MDD), and the non-steady outflow which is also illustrated in the right panel.

is nearly equal to the free-fall velocity. With both  $B_p$  (dipole fields) and  $v_p$  known, the flow and magnetic field structure within the magnetosphere can be derived using these constants with given  $\omega_s$  and  $l$ . One main result regarding this inner magnetosphere (Ghosh et al. 1977) is that, in the case of slow rotators, matter inside the Alfvén surface ( $r_A$ ) rotates in the opposite direction from  $l$ . The reason is that, when  $\omega_s$  has the same sign but is much smaller than  $l/r_A^2$ , the spiral field lines have a forward pitch since field lines are dragged forward by the fast disc rotation. Matter that falls inwards along these spiral fields has a backward azimuthal velocity. These magnetic fields could also spin up the star through the magnetic stress.

Meanwhile, the values of  $l$  along different field lines depend on the condition in the transition zone (inside the screening radius  $R_s$  in Figure 1) where the corotating flow (with  $\mathbf{v}_p$  following  $\mathbf{B}_p$ ) changes to the Keplerian disc flow. Since the flow in the transition zone is neither steady nor axisymmetric, the full angular momentum

equation is needed to describe this region:

$$\frac{\partial R \rho v_\phi}{\partial t} + \nabla \cdot (R(\rho \mathbf{v} v_\phi - \mathbf{B} B_\phi + P \mathbf{e}_\phi)) = 0, \quad (5)$$

where  $P$  is the total pressure. If using spherical-polar coordinates,  $R$  is replaced with  $r \times \sin \theta$ .

Ghosh & Lamb (1979a) built a simple disc model for the transition zone, assuming the accretion can reach a steady state with an effective electrical conductivity ( $\sigma_{eff}$ ) in this region. In a steady state, we have

$$\nabla \times \mathbf{B} = \frac{4\pi \mathbf{J}}{c}, \quad (6)$$

with the Ohm's law  $\mathbf{J} = \sigma_{eff}(\mathbf{E} + (\mathbf{J} \times \mathbf{B})/c)$ . If  $B_\phi$  changes over the disc scale height  $H$ , we have

$$\frac{B_\phi}{H} = \frac{(\Omega - \Omega_s)rB_z}{\eta}, \quad (7)$$

where  $H \equiv c_s/\Omega$  is the disc scale height and  $\eta \equiv c^2/(4\pi\sigma_{eff})$  is the resistivity. The resistivity has to satisfy Equation 7 for a steady state, meaning that the



slippage of field lines balances the azimuthal shear. The azimuthal current screens the background stellar fields. Ghosh & Lamb (1979a) did not specify the source of the resistivity. But if we consider turbulent resistivity  $\eta \sim \nu \sim \alpha H c_s$  and  $\Omega_s = 0$ , we have  $B_\phi/B_z = R/(\alpha H)$ . If  $\alpha < R/H$ ,  $B_\phi$  is then larger than  $B_z$ , and the magnetic pressure from the toroidal fields can drive field inflation until fields open up (Aly & Kuijpers 1990; Lovelace et al. 1995; Uzdensky et al. 2002). These later works suggest that a steady state may not be possible with the turbulent resistivity.

The transition zone is separated into the inner transition zone (also called the boundary layer) where the azimuthal velocity changes dramatically due to the magnetic stress and the outer transition zone where the disc is Keplerian but the residual stellar magnetic fields affect the disc accretion. The boundary between these two transition zones is denoted as  $R_b$  and is a sizable fraction of the Alfvén radius for spherical accretion

$$r_A = r_* \left( \frac{B_*^4 r_*^5}{2GM_* \dot{M}^2} \right)^{1/7} \quad \text{in C.G.S.,} \quad (8)$$

where  $r_A$  is sometimes called the magnetospheric truncation radius  $R_T$  (Hartmann et al. 2016). In this paper, we define  $R_T$  as the radius where the averaged azimuthal velocity drops to half of the local Keplerian velocity ( $v_K$ ). As will be shown later, the azimuthal velocity changes dramatically around the magnetospheric truncation radius. Thus, choosing other velocities between 0 and  $v_K$  for the definition of  $R_T$  barely affects  $R_T$ . In Section 4.2, we will compare our measured  $R_T$  in the simulation with various definitions of the magnetospheric truncation radius, and show that the measured  $R_T$  is quite close to  $r_A$  in Equation 8. The outer transition zone ends at  $R_s$ , where the screening current reduces the background stellar magnetic fields to zero. In the Ghosh & Lamb (1979a) model,  $R_s$  could be tens to hundreds of times larger than  $R_b$ . The broad outer transition zone in their model plays a key role in the coupling between the disc and the star, especially for fast rotators. If the torque on the star is written as

$$T_* = n(GM_* R_b)^{1/2} \dot{M}, \quad (9)$$

Ghosh & Lamb (1979b) derived  $n \approx 1.4$  for a non-rotator. The  $\alpha$  accretion disc (Shakura & Sunyaev 1973) exists beyond the transition zone, and continuously provides mass inwards. Since we focus on the simplest setup with a non-rotator, we will not discuss the rich physical processes associated with moderate and fast rotators (Ghosh & Lamb 1979b; Lovelace et al. 1999; Romanova et al. 2003a, 2004a).

## 2.2. Angular Momentum Transport and Disc Evolution

Our first-principle 3-D simulation reveals that the flow structure is more complicated than that assumed in the

traditional Ghosh & Lamb model. To understand the flow structure in the 3-D simulation, we need to study how angular momentum is transported among different regions. For the disc region that reaches a steady state, the second term in Equation 5 becomes zero. In other words, if we define  $S$  as a surface surrounding the star which is also along the  $\phi$  direction (so  $S$  could be cylinders or spheres surrounding the star), we have

$$\int R(\rho \mathbf{v} v_\phi - \mathbf{B} B_\phi) \cdot d\mathbf{S} = \text{const} \quad (10)$$

along the radial direction. If we assume  $S$  is the cylinder surface around the star, we have

$$R \langle v_\phi \rangle \dot{M} + R \int (\rho v_R (v_\phi - \langle v_\phi \rangle) - B_R B_\phi) dS = \text{const} \quad (11)$$

at different  $R$ . The symbol  $\langle \rangle$  denotes averaging over the  $\phi$  direction, and we have assumed that  $\langle v_\phi \rangle$  is constant along the cylinder. The first and second terms within the integral are Reynolds and Maxwell stresses. Thus, for the steady state, the accretion rate is directly determined by the total stress and the constant. The constant represents the torque between the star and the disc. Considering that  $\langle v_\phi \rangle \sim v_K \sim R^{-1/2}$  and  $\dot{M}$  is constant with  $R$ , the first term on the left-hand side increases with  $R$ . Thus, at large distances, the constant on the right hand side becomes negligible, and the  $\dot{M}$  term is balanced by the stress term. The accretion structure there is solely determined by the stress values. On the other hand, the constant is crucial for the disc's structure at the inner disc edge. We will discuss the constant in detail in §5.2

We can also derive the disc's accretion rate even if the disc has not reached the steady state. We can average the angular momentum equation (Equation 5) in the azimuthal direction to derive

$$\begin{aligned} \frac{\partial R \langle \rho v_\phi \rangle}{\partial t} = & - \frac{1}{R} \frac{\partial}{\partial R} (R^2 \langle \rho v_R v_\phi - B_R B_\phi \rangle) \\ & - \frac{\partial}{\partial z} (R \langle \rho v_z v_\phi - B_z B_\phi \rangle), \end{aligned} \quad (12)$$

If we integrate Equation 12 vertically in the disc region and use the mass conservation equation, we have

$$\begin{aligned} \frac{\partial \int R \langle \rho \delta v_\phi \rangle dz}{\partial t} = & - \frac{1}{R} \frac{\partial}{\partial R} \left( R^2 \int (\langle \rho v_R \delta v_\phi \rangle - \langle B_R B_\phi \rangle) dz \right) \\ & - \frac{\dot{M}_{acc}}{2\pi R} \frac{\partial R v_k}{\partial R} - R (\langle \rho v_z \delta v_\phi \rangle - \langle B_z B_\phi \rangle) \Big|_{z_{min}}^{z_{max}}, \end{aligned} \quad (13)$$

where  $\delta v_\phi \equiv v_\phi - v_k$ <sup>2</sup>. The equation connects the disc's radial mass accretion rate ( $\dot{M}_{acc} = 2\pi R \int \rho v_R dz$ ) to the

<sup>2</sup>  $v_k$  is assumed to be constant along  $z$ . Without this assumption, there will be an additional term related to  $M_{Ioss} \partial v_k / \partial z$ .

$R\phi$  stress within the disc and  $z\phi$  stress at the disc surface. Equation 13 is widely used in accretion disc studies (e.g., Turner et al. 2014). However, it can also be used to study flows in the magnetosphere where the  $v_z$  term describes the vertical flow lifted out of the disc plane. The terms  $\langle \rho v_R \delta v_\phi \rangle$  and  $-\langle B_R B_\phi \rangle$  are the radial Reynolds and Maxwell stresses, and the corresponding  $\alpha$  parameters can be defined as

$$\alpha_{Rey} = \langle \rho v_R \delta v_\phi \rangle / \langle p \rangle \quad \text{and} \quad \alpha_{Max} = -\langle B_R B_\phi \rangle / \langle p \rangle. \quad (14)$$

Stresses and  $\alpha$  parameters in spherical-polar coordinates can be defined in similar ways. If we define the vertically integrated  $\alpha$  parameter as

$$\alpha_{int} = \frac{\int T_{R\phi} dz}{\Sigma c_s^2}, \quad (15)$$

where  $T_{R\phi}$  is the sum of both radial Reynolds and Maxwell stresses, Equation 13 can be written as

$$\dot{M}_{acc} = -\frac{2\pi}{\partial R v_k / \partial R} \times \left( \frac{\partial}{\partial R} (R^2 \alpha_{int} \Sigma c_s^2) + R^2 (\langle \rho v_z \delta v_\phi \rangle - \langle B_z B_\phi \rangle) \right) \Big|_{z_{min}}^{z_{max}}, \quad (16)$$

for a steady state. It is the differential form of Equation 11. Equation 16 suggests that both the internal stress (the radial gradient of the  $r$ - $\phi$  stress) and the surface stress can lead to accretion. To understand the flow structure, We will measure these stresses and  $\alpha$  values directly from our simulations.

### 3. METHOD

We solve the magnetohydrodynamic (MHD) equations in the ideal MHD limit using Athena++ (Stone et al. 2020). Athena++ is a grid-based code using a higher-order Godunov scheme for MHD and constrained transport (CT) to conserve the divergence-free property for magnetic fields. Compared with its predecessor Athena (Gardiner & Stone 2008; Stone et al. 2008), Athena++ is highly optimized for speed and uses a flexible grid structure that enables mesh refinement, allowing global numerical simulations spanning a large radial range.

We adopt a Cartesian coordinate system  $(x, y, z)$  with mesh-refinement to include both the central magnetized star and the accretion disc. Although the spherical-polar coordinate system is normally used for accretion disc studies, its grid cells become highly distorted at the grid poles in this case. Although Athena++ includes a special polar boundary condition to treat these grid cells (Zhu & Stone 2018), they still introduce large numerical errors and significantly limit the evolution timestep. Considering that most accretion onto the star occurs close to the star's magnetic poles, accurately simulating the flow in these regions is crucial. Thus, the Cartesian

coordinate system is better suited for magnetospheric accretion studies. After the simulation is completed, we transform all quantities into spherical-polar coordinates and cylindrical coordinates to simplify the data analysis. In this paper, we use  $(R, \phi, z)$  to denote positions in cylindrical coordinates and  $(r, \theta, \phi)$  to denote positions in spherical polar coordinates. In both coordinate systems,  $\phi$  represents the azimuthal direction (the direction of disc rotation).

Our simulation domain expands from  $-64R_0$  to  $64R_0$  in each  $x, y$ , and  $z$  direction, with 320 grid cells in each direction at the root level.  $R_0$  is the code length unit, which is quite close to the magnetospheric truncation radius  $R_T$  at the end of the simulation. The stellar radius, denoted as  $r_{in}$ , is chosen as  $0.1 R_0$ , so that the magnetospheric truncation radius is roughly 10 times larger than the stellar radius. Static mesh-refinement has been adopted with the fourth level (cells with  $2^4$  times shorter length) at  $[-8, 8]R_0 \times [-8, 8]R_0 \times [-1, 1]R_0$  for  $x \times y \times z$ . Within this fourth level domain, one additional higher level is used for every factor of 2 smaller domain until the seventh level at  $[-R_0, R_0] \times [-R_0, R_0] \times [-0.125R_0, 0.125R_0]$ . Color contours of density and the grid structure for the innermost several levels are shown in Figure 2. If the disc's aspect ratio is 0.1, the disc scale height is resolved by 16 to 32 grid cells at the disc region between  $R = 0.5R_0$  to  $R = 8R_0$ . At the finest level, the cell size is  $0.003125 R_0$ . Piecewise linear method is used in the spatial reconstruction, while Van Leer integrator is adopted for the time integration.

#### 3.1. Disc Setup

The initial density profile at the disc midplane (the  $x - y$  plane) is

$$\rho_d(R, z = 0) = \rho_0 \left( \frac{R}{R_0} \right)^p. \quad (17)$$

In our code unit, we set  $\rho_0 \equiv \rho_d(R = R_0, z = 0) = 1$ , and the time unit  $1/\Omega(R = R_0) = T_0/2\pi$ .  $T_0$  is the orbital period  $T(R)$  at  $R_0$ . Thus,  $T_0$  is also close to the orbital period at the magnetospheric truncation radius. The temperature is assumed to be constant on cylinders

$$c_s^2(R, z) = c_s^2(R = R_0, z = 0) \left( \frac{R}{R_0} \right)^q. \quad (18)$$

where  $c_s = \sqrt{p/\rho}$  is the isothermal sound speed. We choose  $p = -2.25$  and  $q = -1/2$  so that the disc surface density  $\Sigma \propto R^{-1}$ . For the disc temperature, we set  $(H/R)_{R=R_0} = 0.1$ , where  $H = c_s/\Omega_K$ . We note that this disc is thicker than a typical protoplanetary disc at the magnetospheric truncation radius. Simulations for thinner discs are more computationally expensive and will be presented in the future. We have used the adiabatic equation of state with  $\gamma=1.4$ , while an almost instantaneous cooling is applied for each grid cell at every timestep (the thermal relaxation time is  $10^{-5}$  local

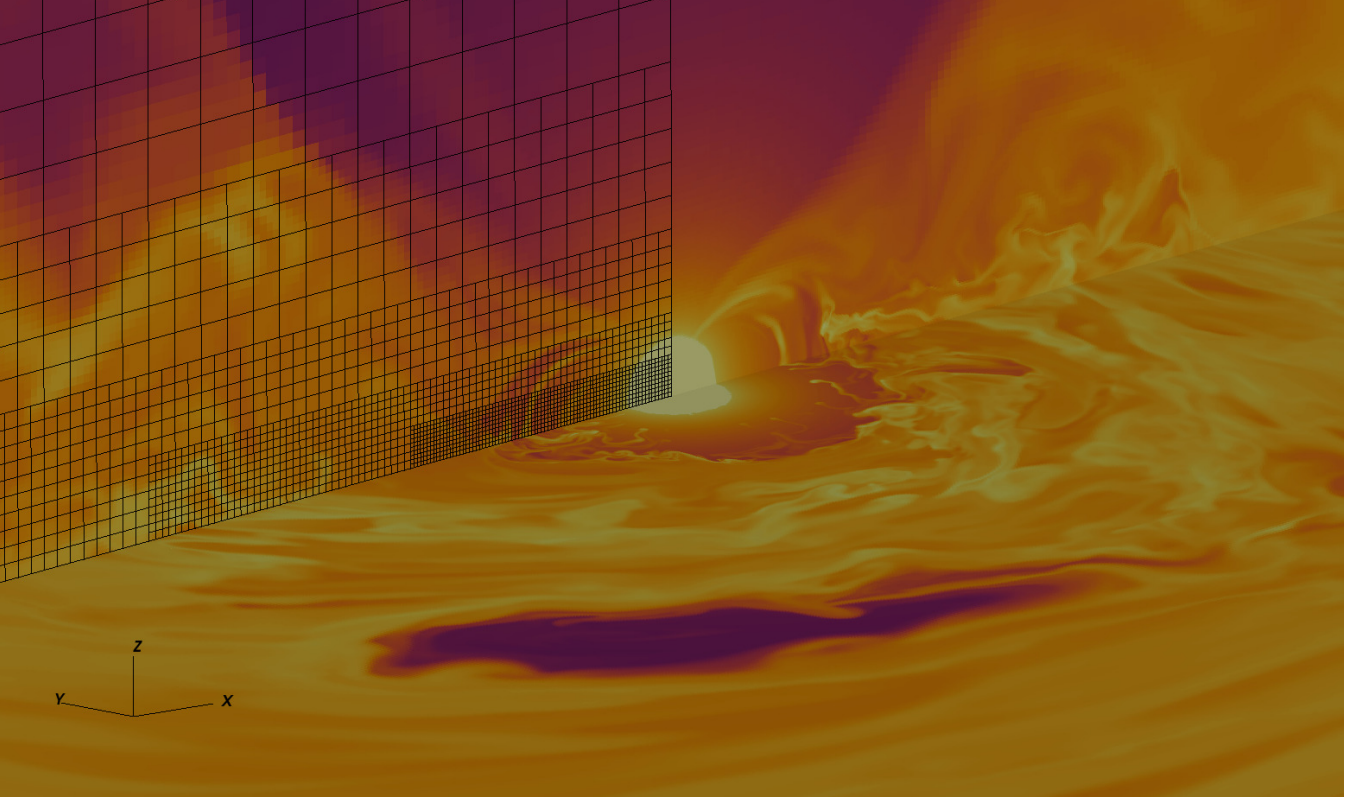


**Figure 2.** Color contours of density at the disc midplane (the  $x$ - $y$  plane) and in a vertical slice (the  $x$ - $z$  plane) at time  $11 T_0$ . The adopted mesh structure is also shown on the left side of the  $x$ - $z$  plane. The movie can be downloaded at [https://figshare.com/articles/media/Magnetospheric\\_Accretion/24103623](https://figshare.com/articles/media/Magnetospheric_Accretion/24103623).

orbital time using the cooling treatment in [Zhu et al. 2015](#)).

The density and velocity in the  $R$ - $z$  plane are set to be

$$\rho_d(R, z) = \rho_d(R, z=0) \exp \left[ \frac{GM_*}{c_s^2} \left( \frac{1}{\sqrt{R^2 + z^2}} - \frac{1}{R} \right) \right], \quad (19)$$

and

$$v_{\phi,d}(R, z) = v_K \left[ (p+q) \left( \frac{c_s}{v_{\phi,K}} \right)^2 + 1 + q - \frac{qR}{\sqrt{R^2 + z^2}} \right]^{1/2}, \quad (20)$$

with  $v_K = \sqrt{GM_*/R}$  (e.g. [Nelson et al. 2013](#)). To avoid the density and velocity becoming infinite at  $R = 0$ , we use  $R = \max(R, r_{in})$  on the right-hand side of Equations 17-20.

### 3.2. Star Setup

The gravitational acceleration from the central star is set as

$$a_r = \begin{cases} -\frac{GM_*}{r^2} \frac{(r-r_{in})^2}{(r-r_{in})^2 + r_{sm}^2} & \text{at } r > r_{in} \\ 0 & \text{at } r < r_{in}, \end{cases} \quad (21)$$

where both the stellar radius  $r_{in}$  and the smoothing length  $r_{sm}$  are set to be  $0.1 R_0$ . At the region with

$R < r_{in}$ ,  $c_s(R, z)$  is set as a constant that is equal to  $c_s(r_{in}, z)$  in Equation 18.

The density and pressure of the star at  $r \leq r_{in}$  are set to be constants as  $\rho(r) = \rho_{*,in}$  and  $P(r) = \rho_{*,in} c_s^2(R = r_{in})$  with a large  $\rho_{*,in}$  value of  $10^7 \rho_0$ . We decrease the disc density by a factor of  $\exp(-(r - r_{mag})^2/r_{sm}^2)$  beyond  $r_{in}$  but within the initial magnetosphere radius  $r_{mag} = 0.5 R_0$ . Then, we add the density of the star that is in pressure equilibrium against the stellar gravity (Equation 21). We first solve

$$\frac{dP(r)}{dr} = a_r(r) \frac{P(r)}{c_s^2(R = r_{in})} \quad (22)$$

from  $r_{in}$  to  $r$ , and then set  $\rho(r) = P(r)/c_s^2(R = r_{in})$ . The velocity structure of the star and the magnetosphere at  $r \leq r_{mag}$  is

$$v_{\phi}(r) = \Omega_* R + v_{\phi,d} \exp(-(r - r_{mag})^2/r_{sm}^2). \quad (23)$$

In this work, we set  $\Omega_* = 0$  as appropriate for a non-rotating star. To maintain the star's structure, we fix the density, velocity, and pressure to be the initial values at  $r < r_{in}$ .

The stellar magnetic field is assumed to be a dipole. Although the magnetic fields of a real star also consist of higher multipole components, the strength of the open

fields and thus the magnetospheric truncation radius are mainly determined by the dipole component (Johnstone et al. 2014). To maintain  $\nabla \cdot \mathbf{B} = 0$ , we use the vector potential  $\mathbf{A}$  to initialize magnetic fields ( $\mathbf{B} = \nabla \times \mathbf{A}$ ):

$$\mathbf{A} = \frac{\bar{\mathbf{m}} \times \mathbf{r}}{r_c^3}, \quad (24)$$

where  $r_c = \max(r, r_{in})$  to avoid the singularity at  $r=0$ . The magnetic moment  $\mathbf{m}$  is thus  $4\pi\bar{\mathbf{m}}$ . Note that the vacuum permeability constant is assumed to be 1 in Athena++, and thus the magnetic pressure is simply  $B^2/2$  in code units. We choose  $\bar{\mathbf{m}} = -0.0447\mathbf{e}_z$  so that the initial plasma  $\beta = 2P/B^2$  at  $R = R_0$  is 10. The fields within the star evolve through numerical diffusion. But at the disc surface  $r_{in}$ , the midplane field strength only decreases by 5% at the end of the simulation.

To avoid small timesteps within the highly magnetized magnetosphere, we employ a density floor that varies with position

$$\rho_{fl} = \rho_{fl,0} \left(\frac{r}{R_0}\right)^p + \rho_{flm,0} \left(\frac{r}{R_0}\right)^{pm}, \quad (25)$$

where  $\rho_{fl,0} = 10^{-5}\rho_0$ ,  $\rho_{flm,0} = 1.33 \times 10^{-5}\rho_0$ , and  $pm = -5.5$ . When  $\rho_{fl}$  gets smaller than  $10^{-9}\rho_0$ , we choose  $10^{-9}\rho_0$  as the density floor. Since the smoothing length ( $0.1 R_0$ ) is resolved by 32 cells at the finest level, the star maintains hydrostatic equilibrium quite well in the absence of magnetic fields. However, the adoption of the high density floor due to the strong stellar magnetic fields leads to inflow onto the star. The density floor is chosen low enough that this inflow is much weaker than the magnetospheric accretion from the disc.

At both the  $x$  and  $y$  boundaries, the flow and magnetic fields are fixed at the initial values during the whole simulation. In the  $z$  directions, we adopt outflow boundary conditions. In the rest of the paper, we drop the code unit (e.g.  $\rho_0, R_0, T_0$ ) after the physical quantities for simplification.

#### 4. RESULTS

We run the simulation for 65 orbits at  $R_0$ , and subsequently, we continue the simulation for another 3.2 orbits albeit with a 10 times smaller  $\rho_{flm,0}$  for the density floor. The total time is equivalent to 2157 Keplerian orbits at the stellar surface  $R_{in} = 0.1$ . The disc has settled to a quasi-steady state, as shown in the right panels of Figure 3 where the disc’s mass accretion rate and one-sided outflow rate are plotted against time. The lower left panel of Figure 3 also shows that the disc accretion has reached a steady state within  $R \sim 6$  at the end of the simulation. The upper left panel of Figure 3 shows a sharp drop in density within the magnetospheric truncation radius,  $R_T \sim 1$ . Beyond this radius, the density at the disc midplane remains relatively constant. In the following subsections, we will present our findings for different regions in the order of the regions’ proximity to the star, starting from the magnetosphere region.

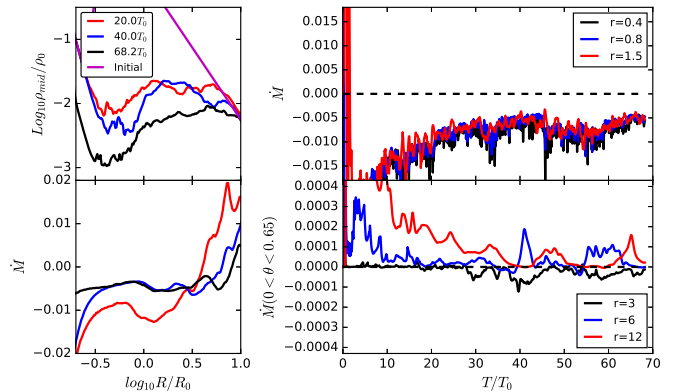


**Figure 3.** Left panels: the disc midplane density and mass accretion rate along the  $R$  direction at three different times. Quantities are averaged over both the azimuthal direction and time (from each time span at 18 to 20  $T_0$ , 38 to 40  $T_0$ , and 66.2 to 68.2  $T_0$ , we average over 21 snapshots). Right panels: the mass accretion rate at  $r=0.4, 0.8, 1.5$  with time (upper panel), and the mass outflow rate at the disc atmosphere (integrated within  $0 < \theta < 0.65$ ) at  $r=3, 6, 12$  with time (lower panel).

#### 4.1. Magnetosphere and Instabilities

The flow within the magnetospheric truncation radius is highly dynamic. Figure 4 shows the contours for the density and magnetic fields at the end of the simulation. In the upper panels of Figure 4, the poloidal plane reveals a distinct contrast in flow structure within and beyond  $R_0 \sim R_T$ . The disc region outside of  $R_0$  is turbulent, with certain denser regions exhibiting  $\beta$  values  $\sim 100$ . In contrast, the region within  $R_0$  appears to be laminar in the poloidal plane and  $\beta$  is less than  $10^{-2}$ . It seems that the material cannot penetrate into the magnetosphere and has to follow the field lines falling onto the star close to the polar directions. However, a different picture emerges from the midplane slices at the lower panels of Figure 4. At the edge of the magnetosphere around  $R_0$ , the disc material becomes filamentary and develops “fingers” that penetrate into the magnetosphere. Due to their higher density, these filaments have higher  $\beta$  values than the rest of the magnetosphere. As they move in, they are lifted and move along the dipole magnetic field lines. In the upper panels of Figure 4, we can see the poloidal cut of these intruding filaments deep inside the magnetosphere. Closer to the star, fewer filaments persist at the midplane (lower panels), as some filaments have been lifted and subsequently accrete onto the star.

To show the development of the filaments, we plot the midplane gas pressure and magnetic pressure at different radii along the azimuthal direction in Figure 5. At the outer edge (e.g.  $r = 6$ ), the gas pressure is within the same order of magnitude as the magnetic pressure. Both pressures fluctuate within one order of



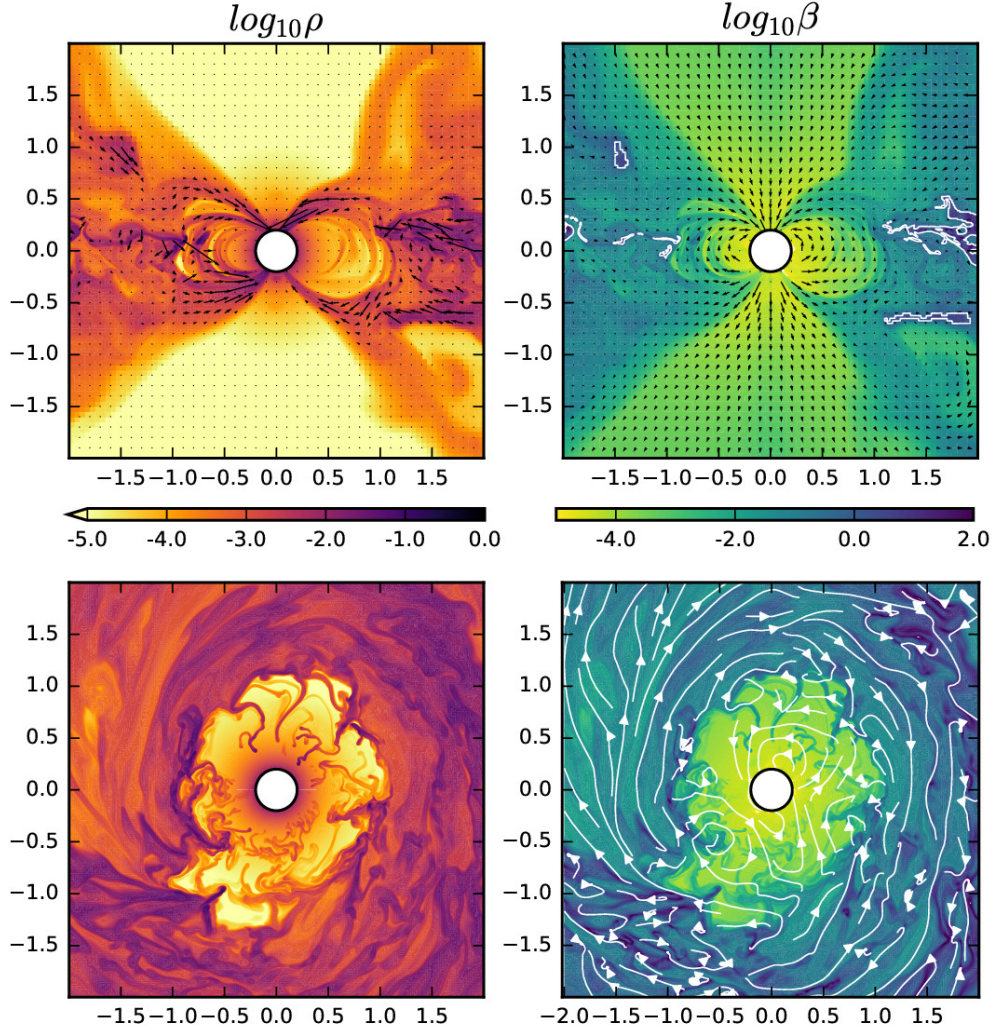


**Figure 4.** Poloidal and midplane slices (upper and lower panels) for density and plasma  $\beta$  (left and right panels) at the end of the simulation. The  $\beta = 1$  contour is also shown as white contours in the upper right panel. Vectors of the momentum and magnetic field are overlotted on the upper  $\rho$  and  $\beta$  panels respectively. The magnetic streamlines are overlotted in the lower right panel.

magnitude with slight anti-correlation (higher  $P_{gas}$  corresponds to lower  $P_B$ ). As  $r$  becomes smaller, magnetic fields become stronger while the gas pressure decreases due to the magnetospheric truncation. This results in a smoother profile of the magnetic pressure but a significant increase in density fluctuations. At  $r = 0.8$ , the density can fluctuate more than 3 orders of magnitude and the gas pressure is near the magnetic pressure only at the highest density peaks. Since the lowest density region has reached the density floor, the real pressure fluctuations are more significant than what is depicted in the plot. Very close to the star (e.g.  $r = 0.4$ ), the magnetic pressure substantially exceeds the gas pressure, even within the densest filaments. With a higher density floor imposed in this region, the density fluctuations within the filaments are less accurately captured.

The density fluctuation is also shown in the upper left panel of Figure 6. At the disc midplane and along  $\theta = 1$ , the amplitude of the density fluctuation (the shaded re-

gion) increases towards the inner disc where the disc magnetic field is stronger. The lower density boundary at  $r \lesssim 1$  is the density floor. Although the density at the midplane has a sharp drop at  $r \sim 1$ , the density profiles at  $\theta = 1$  and  $0.57$  are relatively smooth. This suggests that material high above the disc midplane smoothly accretes into the magnetosphere and onto the star, more similar to the spherical accretion onto a magnetized star. Such smooth transition from the disc to the magnetosphere at higher altitudes is also apparent in Figure 4. Magnetospheric accretion in our simulation seems to be a mixture of the traditional thin disc magnetospheric accretion at the midplane and the spherical accretion above the midplane (more discussion in §4.4).

The “fingers” penetrating into the magnetosphere is due to a type of Rayleigh-Taylor (RT) instability that involves magnetically supported material, called the “interchange instability” (Kruskal & Schwarzschild 1954; Newcomb 1961). Arons & Lea (1976) suggested that this

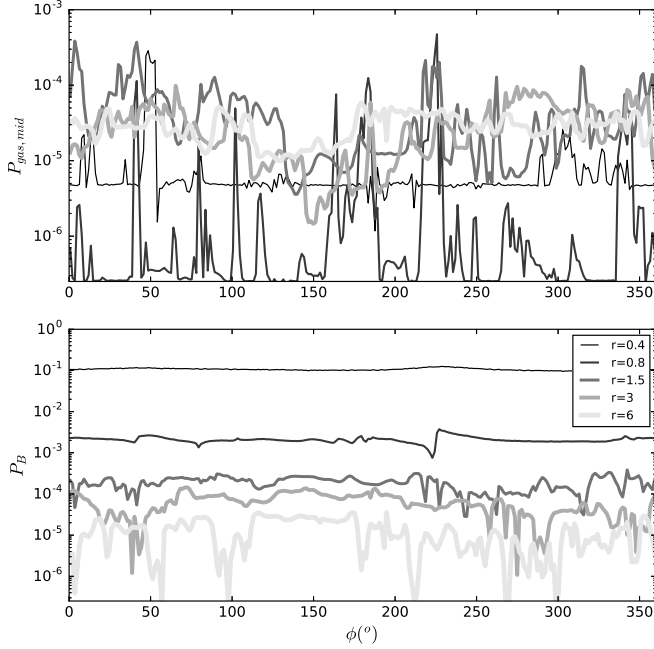


**Figure 5.** The midplane gas and magnetic pressure at different radii along the azimuthal direction at the end of the simulation.

instability can occur at the disc-magnetosphere boundary, which is confirmed later by numerical simulations (Kulkarni & Romanova 2008; Romanova et al. 2008; Blinova et al. 2016). Spruit et al. (1995) has derived the general condition for the instability taking the velocity shear into account, which agrees well with numerical simulations (Romanova et al. 2008; Takasao et al. 2022). For our simulation with a non-rotator, the instability is expected at  $R_T$ . Within the magnetosphere, the flow couples strongly with stellar magnetic fields and its azimuthal velocity reduces to zero (the lower left panel of Figure 6). With such a small azimuthal velocity, the magnetosphere can be considered a hydrostatic fluid supported by magnetic pressure against gravity. This magnetized fluid is unstable when  $-d\rho/dz < \rho^2 g/\gamma P$  (Newcomb 1961), where the gravity is towards negative  $z$ . This condition is identical to the condition of the Rayleigh-Taylor (RT) instability and independent of the field strength. Since the density always increases with  $r$  (opposite to the direction of the gravity) at the boundary between the magnetosphere and the disc due to the magnetospheric truncation, the instability condition is satisfied and the instability develops. In the nonlinear regime of the instability, the material becomes filamentary and sinks to the star (Stone & Gardiner 2007). We caution that, although the instability grows fast in our simulation with a non-rotating star, it will be suppressed for a rotating star (Blinova et al. 2016).

Slightly different from previous simulations, our high-resolution simulation reveals that the filaments have substructures. A larger filament can split into multi-

ple smaller sub-filaments when it moves in, implying a highly dynamic magnetosphere. When the filaments move closer to the star, the magnetic pressure and stress keep increasing and more filamentary material starts to climb vertically along the dipole fields and onto the star. Eventually, most material accretes onto the star at high latitudes.

Once the material begins to follow the field lines, it undergoes a free-fall motion driven by the stellar gravity (Equation 4). To verify the free-fall motion, we plot the averaged radial velocity at different  $\theta$  angles in the upper right panel of Figure 6. The velocity is calculated by dividing the azimuthally averaged radial momentum by the azimuthally averaged density. The thick black solid curve uses the spherically integrated mass flux divided by the spherically integrated density. The thin solid curve is the free-fall velocity starting from  $R_T \sim R_0$ :

$$v_{ff} = \left( \frac{2GM_*}{r} \right)^{1/2} \left( 1 - \frac{r}{R_0} \right)^{1/2}, \quad (26)$$

while the dotted line is the free-fall velocity starting from infinity. Within the magnetosphere, the accretion generally follows the free-fall velocity except for the disc midplane region. At the disc midplane, magnetic fields are in the vertical direction so that the radial inflow is only possible via the interchange instability.

#### 4.2. Transition between the Magnetosphere and the Disc

In the classical model, the magnetosphere and the disc are sharply separated at the magnetospheric truncation radius. Although our simulation supports this sharp transition at the disc midplane, the transition is more gradual and less obvious in the disc atmosphere, especially based on the  $\rho$  and  $v_r$  structure. The upper right  $\bar{v}_r$  panel of Figure 6 shows that, at  $\theta = 1$ , the inflow velocity is still 10% of the free-fall velocity even at  $r \sim 8$ , and the accretion process smoothly transitions from the disc surface accretion to the magnetospheric infall at smaller  $r$  (more discussion on the disc surface accretion in Section 4.4). At  $\theta = 0.57$ , we see mass outflows far away at large  $r$  (Section 4.3).

The distinction between the two regions becomes more pronounced when examining the structure of  $v_\phi$  and  $B_\phi$  in the R-z plane (the lower left two columns of Figure 7).  $v_\phi$  changes from negative values at small  $R$  to positive values in the disc, which is also shown in the lower left panel of Figure 6. The deviation from the Keplerian rotation suggests that the region is more magnetically and less rotationally supported.  $B_\phi$  also changes sign where  $v_\phi$  changes sign (the reason will be discussed in Section 4.4). Furthermore, magnetic fields are mostly poloidal around the star while toroidal in the disc. The different field geometries in these two regions are also shown in the lower right panel of Figure 6 (the  $1/\beta$  panel). Within the disc region ( $R \gtrsim 1$ ), the dominance of azimuthal

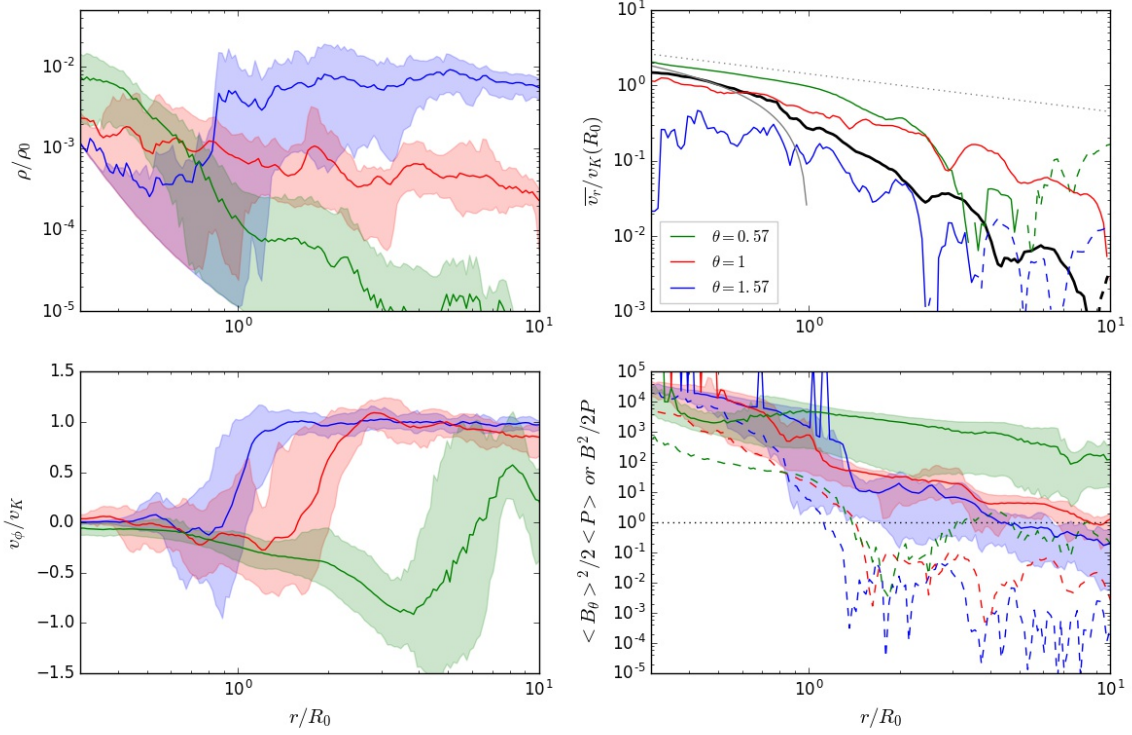


**Figure 6.** The azimuthally averaged density, radial and azimuthal velocities, and  $1/\beta$  along different  $\theta$  directions (different colors) at the end of the simulation. The shaded area shows the quantities within 10% and 90% of all the data along the azimuthal direction. In the  $\bar{v}_r$  panel, the thick black solid curve uses the spherically integrated mass flux divided by the spherically integrated density. The dashed curves in this panel represent negative numbers. The thin solid curve is the free-fall velocity starting at  $R_0$ , and the dotted line is the free-fall velocity starting from infinity. In the lower right panel, the dashed curves are calculated with the azimuthally averaged  $B_\theta$  and pressure, while the solid curves are the azimuthally averaged value of  $1/\beta$  from each cell.

fields is evident from the substantial difference between  $\langle B^2/2P \rangle$  and  $\langle B_\theta \rangle^2/2\langle P \rangle$ . Conversely, at  $R \lesssim 1$ , these two quantities closely align, signifying the dominance of poloidal fields. Magnetic fields are mostly axisymmetric within the magnetosphere ( $\langle B \rangle^2/\langle B^2 \rangle \sim 1$  in the upper right panel of Figure 7). Using azimuthally averaged quantities, we calculate the conserved constants along magnetic field lines ( $k$ ,  $l$ ,  $\omega_s$  from Equations 1 to 3), which are plotted in Figure 7. These quantities are still roughly constant along the streamlines within the magnetosphere, although the density is highly filamentary as shown above. We will discuss the conserved constants in detail in Appendix A.

We have tried various methods to quantitatively define the transition radius between the magnetosphere and the disc. At the disc midplane, we define the transition radius as where  $\Omega = 0.5\Omega_K$ , and consider it as the magnetospheric truncation radius. We measure this radius as  $1.02 R_0$  at the end of the simulation. The magnetospheric truncation radius at the disc midplane has been defined in various ways in the literature. But, for a slow-rotator, we find that they all provide similar values.

The mostly widely used  $R_T$  definition (Equation 8) is derived from  $v_r^2/v_{A,p}^2 = 1$ , or more specifically

$$\rho(R_T)v_r^2(R_T) = \frac{B_p^2(R_T)}{4\pi} \quad \text{in C.G.S.}, \quad (27)$$

where  $v_r = \sqrt{2GM_*/r}$  and  $B_p$  follows a dipole stellar field. This equation can be interpreted in several ways, including ram pressure balancing magnetic pressure, free-fall radial speed equal to the Alfvén speed, or magnetic energy density equal to radial kinetic energy density. In our unit system, we have

$$R_T = \left( \frac{\bar{m}^4 (4\pi)^2}{2GM_* \dot{M}^2} \right)^{1/7}. \quad (28)$$

With our adopted initial dipole fields ( $\mathbf{B}_0$ ) and the measured  $\dot{M} = 0.005$  at the end of the simulation, we can calculate  $R_T = 1.44$ . Considering that the stellar dipole field is  $\sim 0.6 B_0$  around  $R_0$  at the end of the simulation (Section 5.3),  $R_T$  calculated with  $0.6 B_0$  is  $1.07 R_0$ , which is remarkably close to our measured  $1.02 R_0$ . Such a good agreement is due to: 1) the surface radial velocity is indeed close to the free-fall velocity (Figure 6); 2) the dipole field has a very strong radial dependence



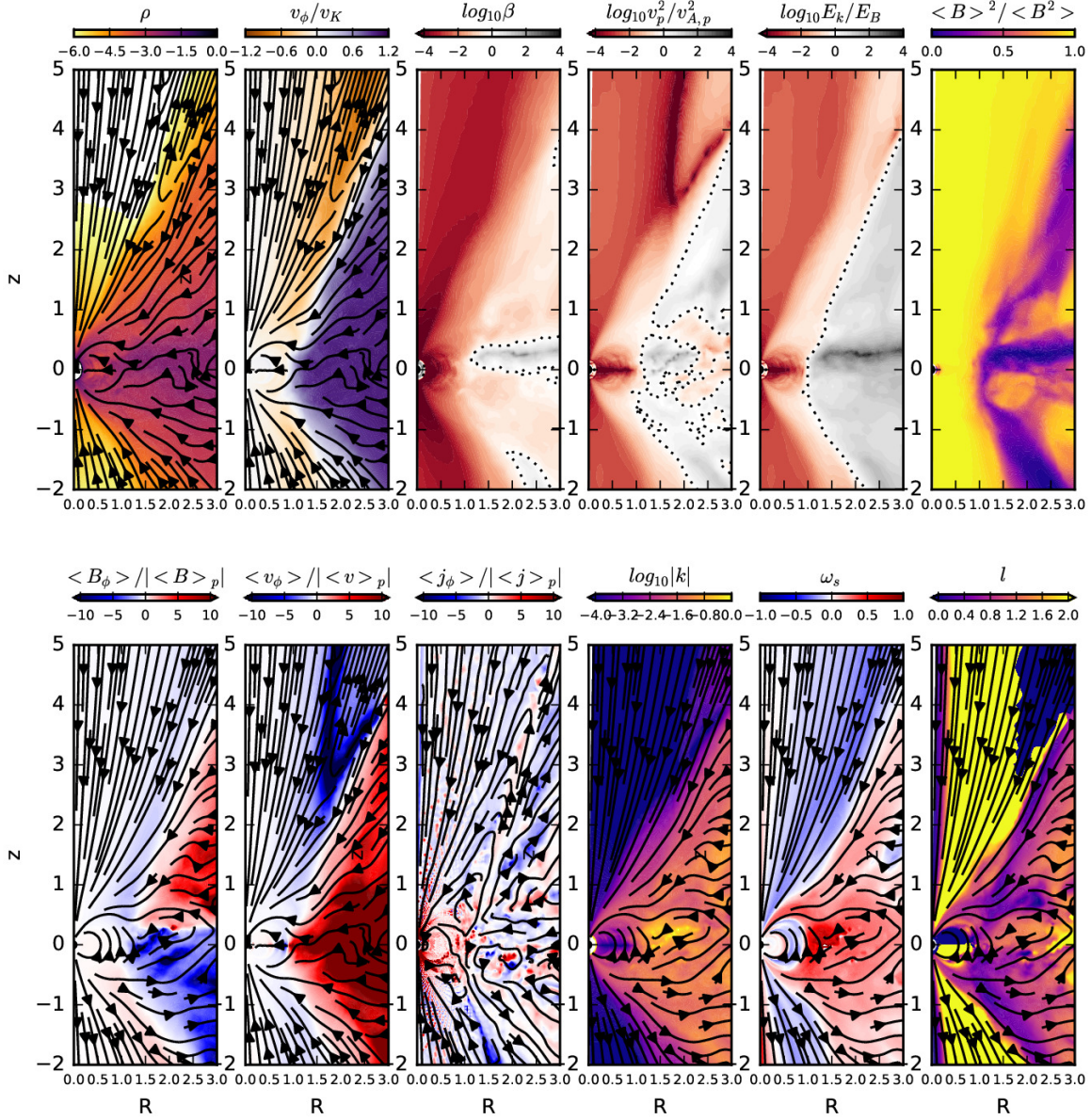


**Figure 7.** Various quantities related to magnetic fields at the end of the simulation. The streamlines of poloidal velocity are shown in the  $\rho$  and  $v_\phi$  panels, while the streamlines of poloidal magnetic field are shown in  $B_\phi$  and  $k$ ,  $\omega_s$ ,  $l$  panels. The streamlines of electric current are shown in the  $j$  panel. The dotted curves in the upper middle 3 panels indicate the regions where the quantity equals zero. Plotted quantities have been averaged over the azimuthal direction except the ones with  $\langle \rangle$  which indicates the azimuthal averaging for specific quantities. For streamlines and  $k$ ,  $\omega_s$ ,  $l$  constants, the primitive variables have been averaged over the azimuthal direction.

( $P_B \propto r^{-6}$ ) so that  $R_T$  has a weak dependence on parameters (Equation 28). Although our derivation is limited to non-rotators, Takasao et al. (2022) find that Equation 28 could also apply to fast rotators.

The other ways to define  $R_T$  include the radius where  $\beta=1$  (Pringle & Rees 1972; Bessolaz et al. 2008; Kulkarni & Romanova 2013), and the radius where the total kinetic energy ( $E_k$ ) equals the magnetic energy ( $E_B$ ) (Lamb et al. 1973). In the  $\beta$ ,  $v_p^2/v_{A,p}^2$ ,  $E_k/E_B$  pan-

els of Figure 7, we see that all three definitions (black dotted curves) give similar  $R_T$  at the disc midplane.

However, when considering regions above the disc midplane, the transition radius between the magnetosphere and the disc exhibits significant variation depending on the method employed. The  $\beta$  panel shows that the magnetic pressure dominates over the thermal pressure in most regions except for the disc midplane and high above the surface where  $B_\phi$  changes sign. The  $v_p^2/v_{A,p}^2$  panel shows that the disc surface (with a high



infall velocity and weak fields) has super-Alfvénic speed but with some sub-Alfvénic patches. Among these three diagnostics,  $E_k/E_B = 1$  provides the clearest separation between the disc and highly magnetized regions. This  $E_k/E_B = 1$  boundary also corresponds to the boundary where  $B_\phi$  and  $v_\phi$  change sign in the disc’s atmosphere. Therefore, we consider  $E_k/E_B = 1$  as the boundary that effectively separates the magnetosphere region from the disc region.

#### 4.3. Magnetically Disrupted Disc and Outflow

Although the disc is pressure supported, the strong magnetization makes this region highly dynamic, occasionally leading to magnetic disruptions in some regions. Magnetic reconnection and interchange instability could sometimes reorganize magnetic fields around the truncation radius, leading to a large-scale density void (the middle panels of Figure 8). Before the density void forms,  $B_\phi$  changes sign 3 times when transitioning from one side of the disc to the other (bottom panels). While the density void is forming, the magnetic fields on both sides of the disc directly connect with each other ( $49 T_0$  panel in the bottom row). The void starts at the magnetospheric truncation radius and expands outwards. The outward motion slows down around 2-3  $R_T$  and the void orbits around the central star at sub-Keplerian speed. As shown in Figure 8, it takes 6  $T_0$  for the density void to finish one orbit, while the Keplerian orbital timescale at  $R = 2$  is only 2.8  $T_0$ . This suggests that the asymmetric density structure is magnetically connected to either the region at larger scales with a slower Keplerian speed or the region within the magnetosphere which also rotates slowly. The magnetic field lines are shown in the bottom rows of Figure 8, where the density void is connected with the strong azimuthal magnetic fields at the disc surface and these magnetic fields rise up and outwards with time. When the magnetic bubble rises, it opens field lines and drives outflow.

These density voids and magnetic islands are remarkably similar to those in models of magnetically arrested discs (MAD, Tchekhovskoy et al. 2011). The density voids in MAD discs are similarly associated with flux tubes which move outwards until the circularization radius, and eventually dissipate after several orbits (Porth et al. 2021). These voids appear quasi-periodically, regulating the spin-up/down of the central blackhole and outflow rates, which may be associated with the flares of Sgr A\*. Similarly, these voids due to the strong disc fields have also been invoked to explain the giant flares in protostars (Takasao et al. 2019). On the other hand, it is essential to highlight that magnetospheric accretion differs from the MAD state around BHs or discs threaded by external vertical fields. In magnetospheric accretion, mass in the disc accretes to the central star following the stellar field lines after mass is loaded into these field lines through turbulence or reconnection processes. In contrast, in the MAD state or discs with

net vertical fields, there is no field line connecting the disc and the central object. Hence, we choose to designate our observed disc state, characterized by the presence of magnetically buoyant bubbles during the magnetospheric accretion, as the magnetically disrupted disc (MDD) rather than categorizing it as the MAD state.

In our simulations, it is also evident that the appearance of magnetic islands is related to subsequent disc mass ejection/outflow events. As shown in Figure 8, the magnetic islands are magnetically connected to the disc surface, generating strong negative  $B_\phi$  at  $z > 0$ . The magnetized “bubble” at the disc surface moves out (bottom panels), and pushes material outwards (top panels), leading to asymmetric non-steady outflow. Such an outflow event is also shown in the  $\dot{M}(0 < \theta < 0.65)$  panel of Figure 3 as the bumps on the blue and red curves. At  $r = 6$ , the outflow rate starts to rise at  $t=55 T_0$  and drops down at  $t=63 T_0$ , which corresponds to the time interval in Figure 8. It takes time for the ejection to move to larger distances. At  $r = 12$ , the outflow rate rises at  $t=65 T_0$ .

On the other hand, in our simulation that includes a non-rotating central star, the outflow rate is small compared with the accretion rate even during these mass ejection events. Even including outflow from both sides of the disc, the outflow rate during these mass ejection events ( $\dot{M} \sim 0.0002$  based on Figure 3) is less than 5% of the disc accretion rate ( $\dot{M} \sim 0.005$ ). Such a small outflow rate is due to the magnetic field structure in the low density region surrounding the non-rotating star (Figure 7). At one side of the disc (e.g.  $z > 0$  at  $R = 2$ ), all magnetic field lines are pointing towards the star. The material at the disc surface is channeled towards the star directly, and cannot move across the field lines to be loaded to the low density region high above the disc. Furthermore, even if the material can slip into the low density region, the material will simply fall to the star following the field lines. This occurs due to the magnetic fields being connected to the non-rotating star, and as a result, the flow lacks any rotation and centrifugal support. Due to this latter reason, it is not even clear if the mass ejection seen in Figure 8 can eventually escape the system. In contrast, we expect significantly higher outflow rates for rotating stars. Mass loaded into the stellar open fields, either by some steady diffusion or by the magnetic “bubbles”, could be accelerated by twisted stellar magnetic fields (Matt & Pudritz 2005). However, the outflow in this case depends on the density structure around the star (e.g. from the stellar wind) which is highly uncertain.

#### 4.4. Surface Accretion and Disc Evolution

Our grid setup enables us to evolve the disc for a long timescale (2157 Keplerian orbits at the stellar radius) with a reasonable computational cost. The disc outside the magnetosphere has reached a steady state over a large dynamical range ( $R \lesssim 6R_T$ ). To study the steady

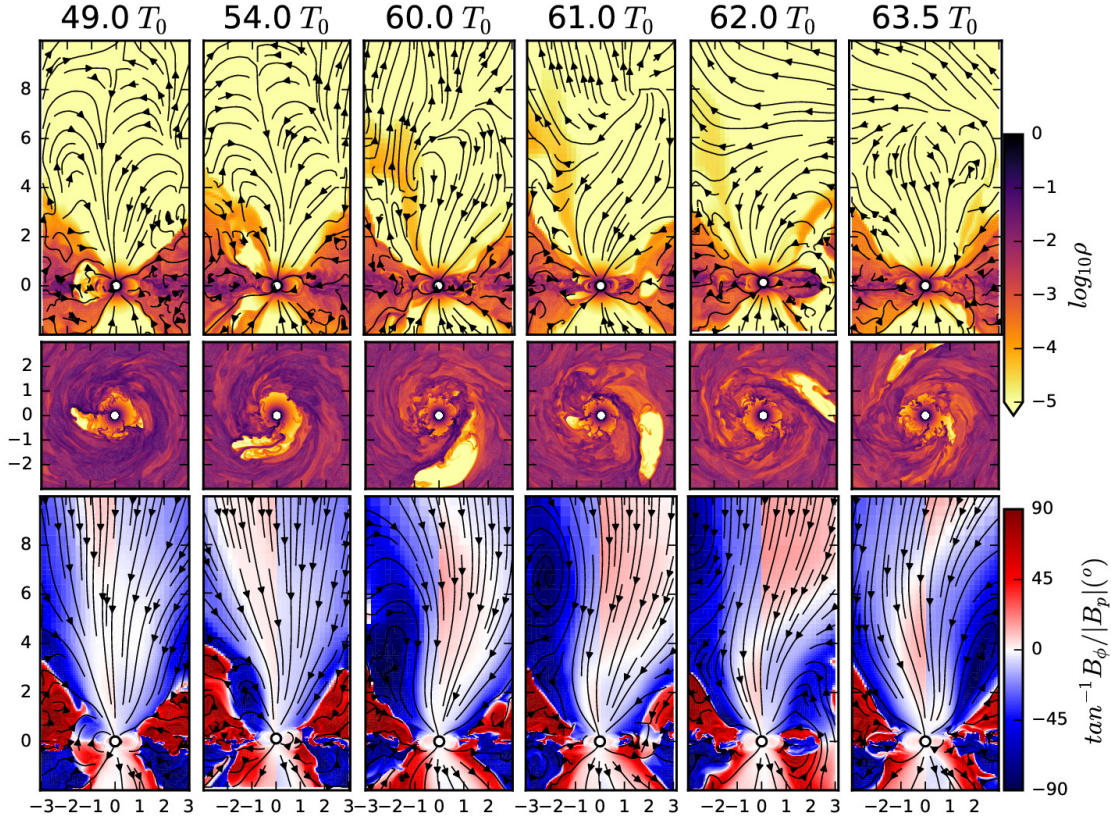


**Figure 8.** The density (upper and middle panels) and  $B_\phi$  (lower panels) structure at different times, highlighting the density void in the disc. The vectors in the upper and lower panels are the velocity and magnetic field vectors respectively. While the upper and lower panels show the poloidal cut, the middle panels show the midplane cut. The movie can be downloaded at [https://figshare.com/articles/media/Magnetospheric\\_Accretion/24103623](https://figshare.com/articles/media/Magnetospheric_Accretion/24103623).

disc accretion, we plot the radial profiles of surface density, stress,  $\alpha$ , and magnetic fields in Figure 9. The  $r$ - $\phi$  stress changes sign within the magnetospheric truncation radius, mainly due to the reversal of  $B_\phi$ . Beyond  $R_0 \sim R_T$ , the midplane  $r$ - $\phi$  stress decreases as  $R^{-2}$ , so that the midplane  $\alpha_{r\phi}$  changes as  $R^{-1.5}$ . The vertically integrated  $\alpha_{int}$  (Equation 15) changes as  $R^{-2}$  and  $\Sigma$  changes as  $R$ . With these profiles,  $\dot{M}$  is constant with  $R$  (Equation 16) if we ignore the stresses at the disc surface (which will be justified in Appendix B). We note that these profiles are significantly different from those in Zhu & Stone (2018) where the disc is threaded by net vertical magnetic fields with a constant initial  $\beta$ . However, the disc accretion rates in both cases are constant radially. The disc in Zhu & Stone (2018) has  $\Sigma \propto R^{-0.6}$  and  $\alpha_{int} \propto R^{-0.4}$ , which also leads to a constant  $\dot{M}$  along  $R$ . This suggests that an MHD turbulent disc with net vertical magnetic fields (either from the star or molecular cloud) can reach different steady states depending on the initial magnetic field distribution and field transport within the disc. The disc evolution is inconveniently affected by the global magnetic field structure that is difficult to be constrained for real astrophysical systems. The magnetic fields adjust themselves quickly and affect

the disc structure at a very short timescale, as indicated by Zhu & Stone (2018).

While we lack a comprehensive theory to explain the observed differences in the smaller  $\alpha$  slope and the higher  $\Sigma$  slope in this study compared to those in Zhu & Stone (2018), we can offer a preliminary explanation based on stress considerations. To reach a steady state, the vertically integrated stress needs to follow  $R^{-1.5}$ , independent from the external field configurations, which means  $\alpha_{int}\Sigma \propto R^{-1}$  with our temperature profile. Since the net vertical fields in this work decrease much faster outwards compared with those in Zhu & Stone (2018), the midplane  $\beta$  increases faster outwards even with the same surface density profile, which leads to a faster decrease of  $\alpha_{int}$  moving outwards (indicating a smaller slope or a more negative slope). Since  $\alpha_{int}\Sigma$  needs to maintain the same  $R^{-1}$  slope,  $\Sigma$  needs to increase faster outwards (indicating a higher slope), which drives an even steeper  $\beta$  and a smaller  $\alpha$  slope. Eventually, a balance is achieved with a small  $\alpha_{int}$  slope and a high  $\Sigma$  slope. To derive the exact slope values, we need to understand how field is transported and amplified in the disc. Such an analytical model has not been constructed. We hope that our simulations here could shed light on how to construct such a model in future.



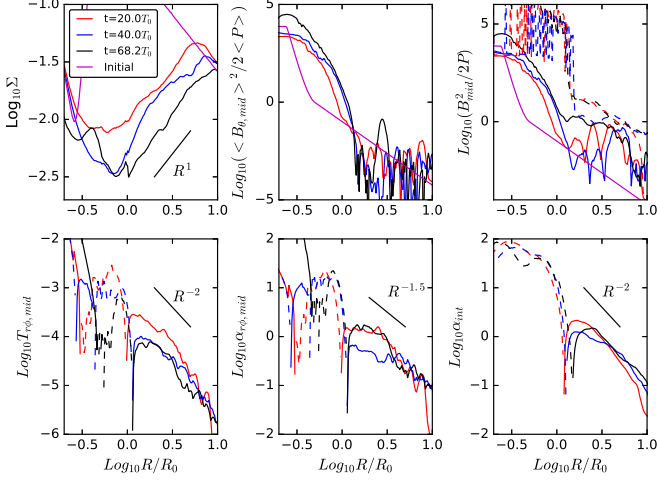


**Figure 9.** The disc surface density,  $\langle B_{\theta, mid} \rangle^2/2\langle P \rangle$ ,  $B_{mid}^2/2P$  (upper panels), midplane  $r$ - $\phi$  stress, midplane  $\alpha_{r\phi}$ , vertically integrated  $\alpha_{int}$  (lower panels) along the  $R$  direction at different times. The dashed curves in the lower panels represent negative values. In the upper right panel, the solid curves are  $\langle B_{mid} \rangle^2/2\langle P \rangle = (\langle B_{r, mid} \rangle^2 + \langle B_{\theta, mid} \rangle^2 + \langle B_{\phi, mid} \rangle^2)/2\langle P \rangle$ , while the dashed curves are  $\langle B_{mid}^2/2P \rangle$ . All plotted quantities are averaged over both the azimuthal direction and time (from each time span from 18 to 20  $T_0$ , 38 to 40  $T_0$ , and 66.2 to 68.2  $T_0$ , 21 snapshots are averaged). The quantities with  $\langle \rangle$  are azimuthally averaged first, and then the plotted quantities are averaged over time.

We could also estimate the  $\alpha$  value by equating the viscous timescale at  $R \sim 6$  to the simulation time. The derived  $\alpha$  value is on the order of unity, similar to  $\alpha_{int}$  derived above. This high  $\alpha$  value has important implications for planet formation theory (Section 5.4).

The most surprising feature in our simulation is the vertically extended surface accretion region at  $R \gtrsim R_T$ , as shown in the middle panel of Figure 10. This region is magnetically supported (Figure 11), and is remarkably similar to the surface accretion region in the MRI turbulent discs with net vertical magnetic fields (e.g., Zhu & Stone 2018; Mishra et al. 2020; Jacquemin-Ide et al. 2021). The region extends to  $z \sim r$  and the flow in the region moves inwards supersonically. It is supported by magnetic pressure and located beyond the  $\langle \beta \rangle = 1$  surface. The strong magnetic fields are generated by the azimuthal stretching of the radial magnetic fields from the Keplerian shear. The resulting large  $B_r B_\phi$  stress from net magnetic fields drives the surface accretion, while, at the disc midplane where  $\langle \beta \rangle \gtrsim 1$ , the disc is turbulent due to MRI. The magnetically dominated surface is similar to that in the magnetic elevated disc model (Begelman & Armitage 2023) and the failed disc wind in accretion discs around weakly magnetized stars (Takasao et al. 2018).

To see the similarities and differences between accretion discs threaded by dipole versus net vertical mag-

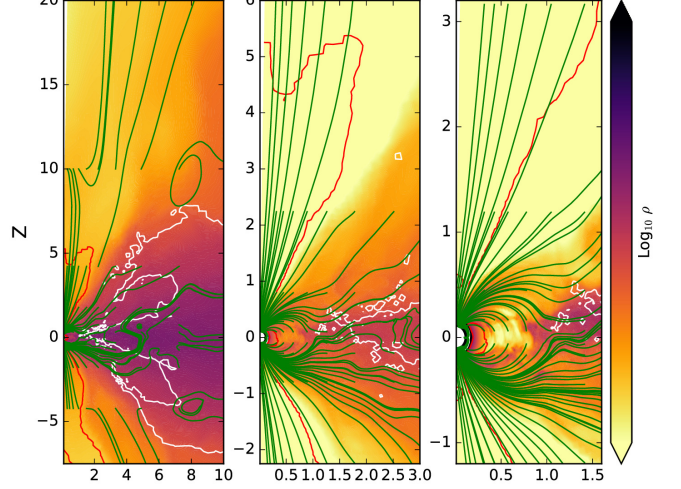


**Figure 10.** Azimuthally averaged density at different scales at  $t = 68.2T_0$ . The green curves are the velocity streamlines calculated with azimuthally averaged velocities. The white curves label where the azimuthally averaged  $\beta = 1$ . The red curves label where the azimuthally averaged density is only larger than the density floor by 10%, indicating that the majority of grids have reached the density floor there. Only the pole region has reached the density floor. The range of the colorbar is  $[-8, 1]$ ,  $[-5, 1]$ ,  $[-3.5, -1]$  in the left, middle, and right panels.

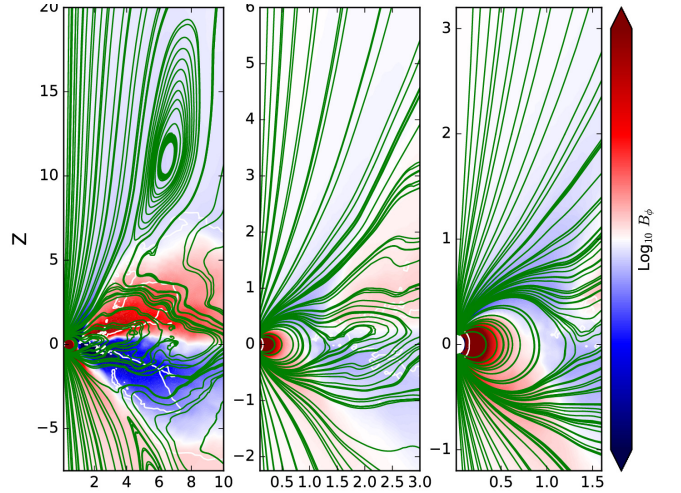


**Figure 11.** Similar to Figure 10 but for  $B_\phi$ , and the green curves are the magnetic streamlines. The range of the colorbar is  $[-0.01, 0.01]$ ,  $[-0.1, 0.1]$ ,  $[-0.1, 0.1]$  in the left, middle, and right panels.

netic fields, Figure 12 compares this magnetospheric accretion simulation against the simulation in Zhu & Stone (2018) where the disc is threaded by net vertical fields with an initial  $\beta_0 = 10^3$ . The magnetically-dominated accreting surface is evident in both simulations. Significant radial inflow at the disc surface can be seen in the  $\langle r^2 \rho v_r \rangle$  panels. It is driven by the high  $r$ - $\phi$  stress

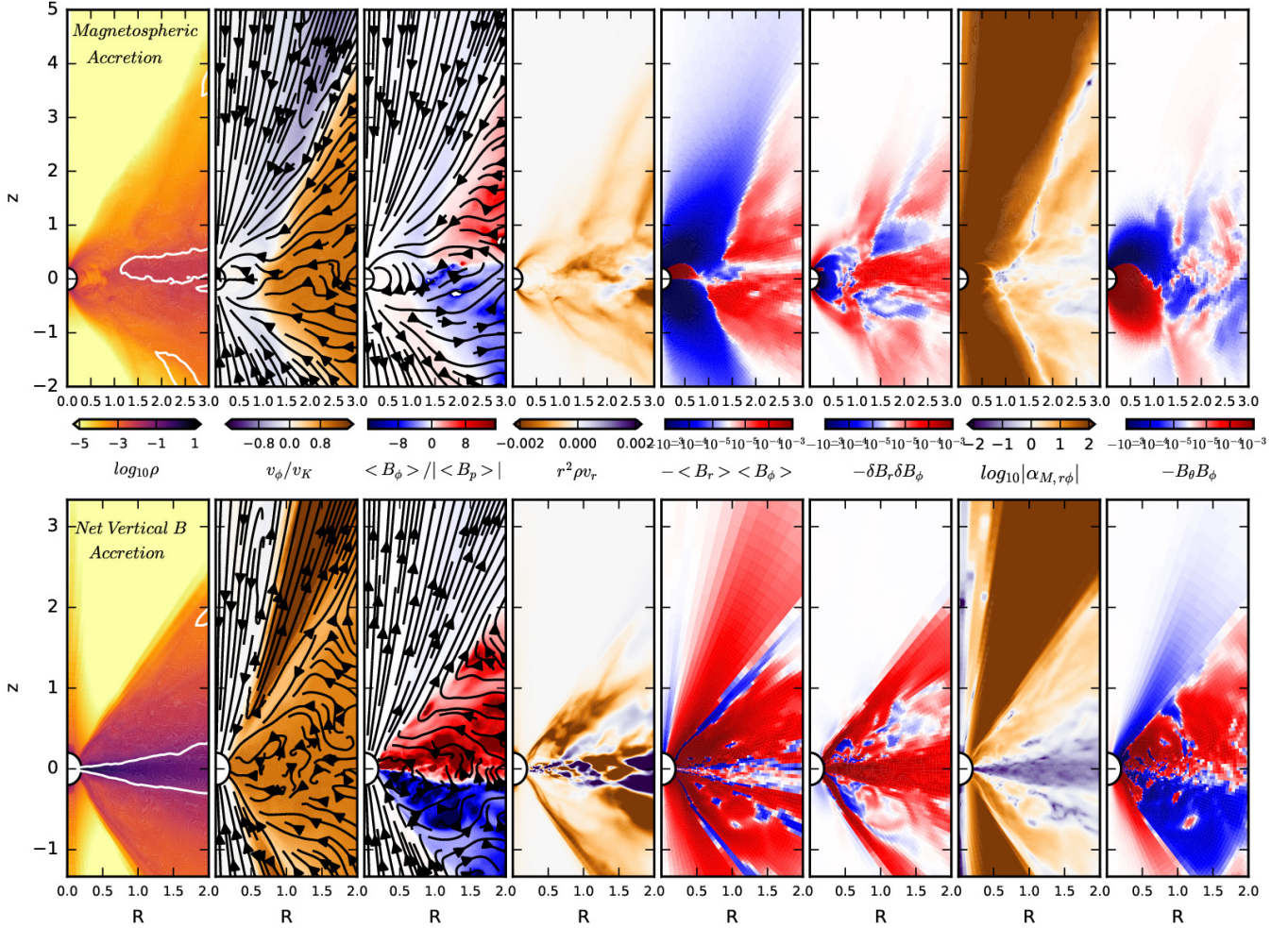


**Figure 12.** Disc structure from this work (upper panels), compared to the structure of a disc threaded by net vertical magnetic fields (lower panels, from [Zhu & Stone 2018](#)). Both simulations are shown at the final output, and all plotted quantities are azimuthally averaged. The white contours in the leftmost panels (the density panel) represent where  $\langle \beta \rangle = 1$ . The streamlines in the  $\langle v_\phi \rangle$  panels show the poloidal velocity, while the streamlines in the  $\langle B_\phi \rangle$  panels show the poloidal magnetic fields.

(the  $\langle B_r \rangle \langle B_\phi \rangle$  panel) that is produced by stretching the radial fields azimuthally. The radial fields in magnetospheric accretion come from the stellar dipole fields after reconnection events (the  $\langle B_\phi \rangle$  panel). On the other hand, the radial fields in the net vertical field simulations come from the surface accretion itself, which drags the fields at the surface inwards tilting the vertical fields into the horizontal direction. The magnetic fields also connect the midplane with the disc atmosphere vertically in both cases. The  $B_\theta B_\phi$  stress acts like magnetic braking, which removes angular momentum from the surface to the midplane (the  $\langle B_\theta B_\phi \rangle$  panels). Thus, the  $B_\theta B_\phi$  stress increases surface accretion further while it slows down the midplane’s radial inflow (or even makes it move outwards). On the other hand, the  $B_\theta B_\phi$  stress within the disc can only redistribute angular momentum vertically within the disc, and it cannot lead to the overall disc accretion if we integrate the disc accretion rate vertically throughout the disc. The overall accre-

tion is led by the  $r\text{-}\phi$  stress integrated vertically within the disc and the  $\theta\text{-}\phi$  stress at the disc surface (Equation 16). The simulations in [Zhu & Stone \(2018\)](#) show that the  $r\text{-}\phi$  stresses play a more important role than the  $\theta\text{-}\phi$  stresses at the disc surface, which is also the case for magnetospheric accretion presented here (more details in Appendix B).

[Jacquemin-Ide et al. \(2021\)](#) discover that, for discs threaded by net vertical fields, the surface accretion region consists of two parts: the laminar region at lower  $z$  where the net fields ( $\langle B_r \rangle \langle B_\phi \rangle$ ) dominate the angular momentum transport and the turbulent region at higher  $z$  where the turbulent fields ( $\delta B_r \delta B_\phi$ ) dominate the transport. This is also shown in our Figure 12. They identify that the turbulent region at  $z \sim R$  is due to MRI when the net azimuthal fields become weaker than the net vertical fields. For our magnetospheric accretion simulation, we also detect the turbulent surface accretion region above the laminar region. Turbulent stress



is also observed in the vicinity of the magnetosphere, which could be attributed to the interchange instability. However, it's worth noting that the turbulent stress is significantly weaker than the laminar stress in that region.

The most noticeable differences between these two models are mainly at the magnetosphere and the lowest density region at  $z > r$ . In the upper panels of Figure 12, the stellar dipole fields in the low-density region are pointing toward the star. Since the star is non-rotating, the stellar field lines can magnetically break the low-density region, leading to accretion onto the star instead of launching outflows. As discussed in Section 2.1, for an axisymmetric steady flow around a non-rotating star, the gas velocity and the magnetic field lines are along the same direction ( $B_\phi/B_r \sim v_\phi/v_r$ ). High above the disc at  $z > 0$ ,  $B_\phi$ ,  $B_r$ ,  $v_\phi$ , and  $v_r$  are all negative ( $\langle v_\phi \rangle$  and  $\langle B_\phi \rangle$  panels). Thus, the flow falling onto the star is in the opposite azimuthal direction from the direction of the Keplerian rotation, similar to the traditional picture in Section 2.1. In contrast, for discs threaded by net vertical magnetic fields shown in the lower panels, the net vertical field lines at the disc surface are tilted away from the star. The material in the disc surface connects to the higher and outer low density region magnetically. Since the disc rotates faster than the higher and outer low density region, the magneto-centrifugal wind is launched.

Such quasi-steady structure is not established instantaneously, it is important to understand how the disc evolves to such a state from the initial condition. Such evolution may have implications for outbursting discs. Figure 13 shows the density, velocity, and magnetic structure at different times. In the initial condition, we set up a disc that is in hydrostatic equilibrium with the stellar gravity threaded by a dipole magnetic field. Due to the azimuthal shear, the poloidal fields are quickly stretched to produce toroidal components. The second panel in the third row shows that, inside the matter dominated disc region ( $\bar{\beta} \geq 1$ ), the faster rotation at the inner disc drags the magnetic field with negative  $B_R$  at  $z > 0$  to develop a positive  $B_\phi$  component. On the other hand, in the magnetically dominated region ( $\bar{\beta} < 1$ ) close to the star, the flow's rotation is slowed down by magnetic fields from the non-rotating star (the second panel in the second row). Since the Keplerian rotating disc with  $\bar{\beta} \geq 1$  is outside the magnetosphere with  $\bar{\beta} < 1$ , magnetic fields with negative  $B_R$  in the magnetosphere are stretched to develop the negative  $B_\phi$  component. The strong shear quickly amplifies  $B_\phi$ , especially at the  $\bar{\beta} \sim 1$  region.

The increasing magnetic pressure starts to push material outwards (the third and fourth panels in the second row), forming an outwardly moving magnetic bubble that stretches the magnetic fields in the radial direction (the third row). Such strong magnetic fields in the atmosphere push the  $\bar{\beta} \sim 1$  curve further into the

disc region (the fourth panel in the first row). After the magnetic bubble moves outwards, the field lines open up, similar to the “X-wind model” (Shu et al. 1994). Later, magnetic field lines at the base reconnect so that once again they connect the disc region to the star (the fifth and sixth panels in the third row). This is very similar to the unsteady field inflation model in Lynden-Bell & Boily (1994); Lovelace et al. (1995); Uzdensky et al. (2002). However, unlike these previous studies which are built upon  $R$ - $z$  2-D models, after this initial relaxation stage, our disc generates magnetically supported and turbulent surface regions, which expand with time and allow the disc to accrete quasi-steadily. The difference on the steadiness of accretion is due to the operation of various 3-D instabilities in our simulation, including the magnetic interchange instability around  $R_T$  and the MRI in the outer disc. These instabilities allow field lines to diffuse across disc material, acting like a large anomalous resistivity. Thus, open field lines return to the dipole configuration due to the anomalous resistivity. With a large resistivity, the slippage of field lines balances the azimuthal shear, allowing a quasi-steady accretion (Ghosh & Lamb 1979a). The  $B_\phi$  in the disc atmosphere increases steadily due to the Keplerian shear until the field growth is balanced by turbulent diffusion. This whole process is self-similar at different radii, and eventually the poloidal field structure looks similar to the initial dipole structure except with a very strong azimuthal component. Even at the end of the simulation, the largest scale (e.g. the leftmost panels in Figures 10 and 11) is still far from steady state. Instead, the flow and magnetic structure there look like the structure at  $R \sim 1$  when  $t = 5T_0$  (Figure 13), demonstrating that the flow and magnetic structure expand self-similarly with time.

## 5. DISCUSSION

### 5.1. Comparison with Observations: Filling Factor and Variability

Observable accretion signatures of classical T-Tauri stars are produced within the magnetosphere (Hartmann et al. 2016). The accretion shock at the surface of the star produces the excess emission at ultraviolet, which is the most robust tracer for estimating the disc's accretion rate. Atomic lines are produced over a large volume (probably covering the whole magnetosphere) and the line shapes can be used to constrain the flow structure within the magnetosphere. Detailed radiative transfer modeling reveals that: 1) the maximum infall velocity onto the star is roughly consistent with free-fall velocity (Hartmann et al. 1994; Muzerolle et al. 1998, 2001; Kurosawa et al. 2011); 2) the infall is at moderate latitudes from the disc plane but not at the poles (Bonnell et al. 1998; Muzerolle et al. 1998); 3) the covering factor of the accretion columns at the stellar surface (called “filling factor”) is 0.001 to 0.1 (Calvet & Gullbring 1998); 4) the outflow rate (with 100 km/s ve-

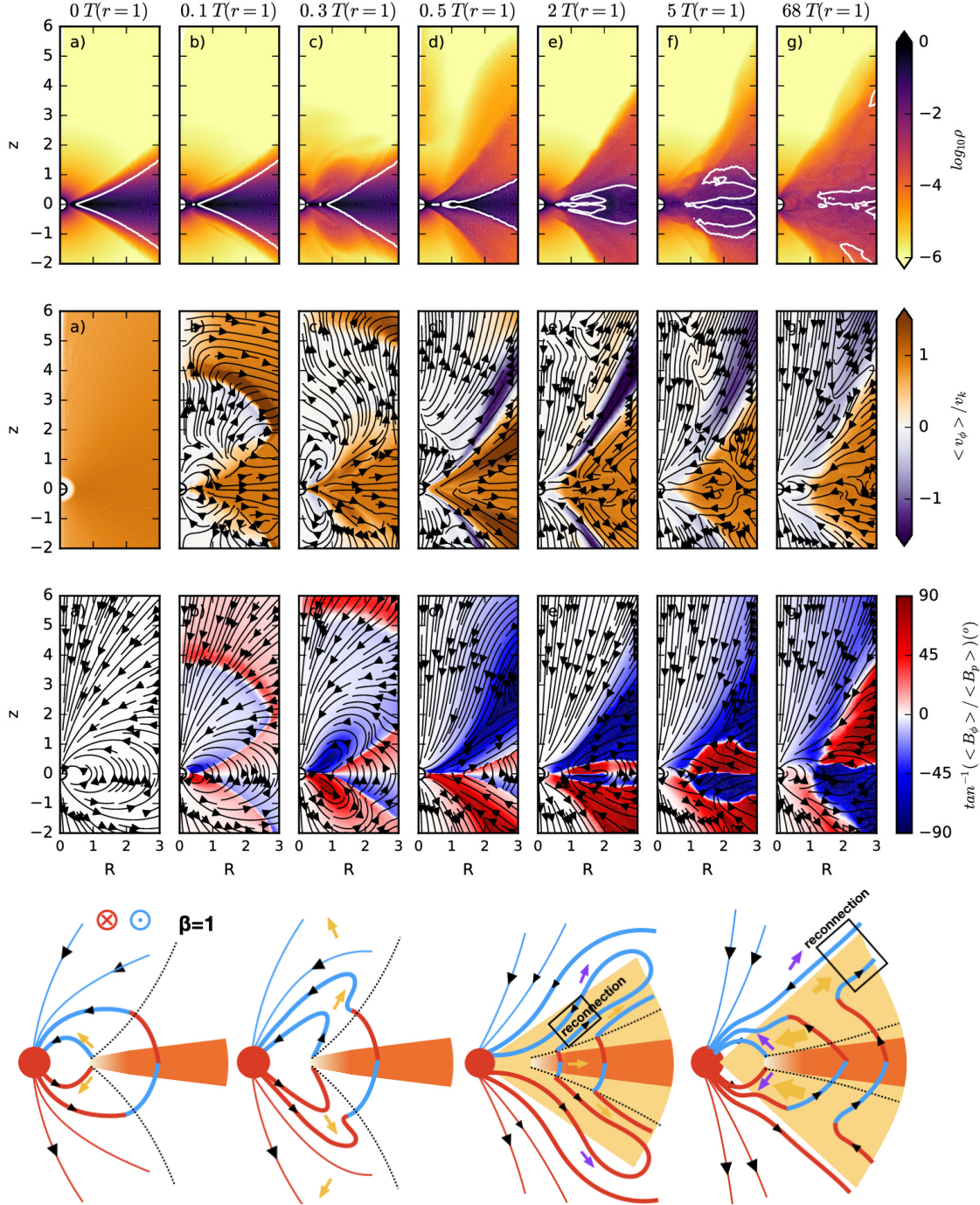


**Figure 13.** Top three rows: the disc density, velocity, and magnetic structure at different times during the simulation (left to right panels). The white contours in the top panels label where  $\bar{\beta} \equiv 2\langle P \rangle / (\langle B_r \rangle^2 + \langle B_\theta \rangle^2 + \langle B_\phi \rangle^2) = 1$ . The streamlines in the panels of the second row represent the poloidal velocity, while the streamlines in the panels of the third row represent the poloidal magnetic field. The bottom row: the schematic diagrams showing how magnetic fields and flow structure change with time. The red and blue curves are magnetic field lines with positive and negative  $B_\phi$  components. The arrows show the flow in the poloidal direction, and their colors (yellow or purple) represent positive and negative  $v_\phi$  in the region.

locity) is correlated with disc accretion rate (Hartigan et al. 1995; Rigliaco et al. 2013; Natta et al. 2014).

We can compare the flow structure in our simulated magnetosphere with above observed properties. Phys-

ical quantities on the  $\theta$ - $\phi$  plane at different radii are shown in Figure 14. The top two rows clearly demonstrate that the material is lifted from the disc (the  $r = 1.6$  panel) to higher altitudes within the magne-

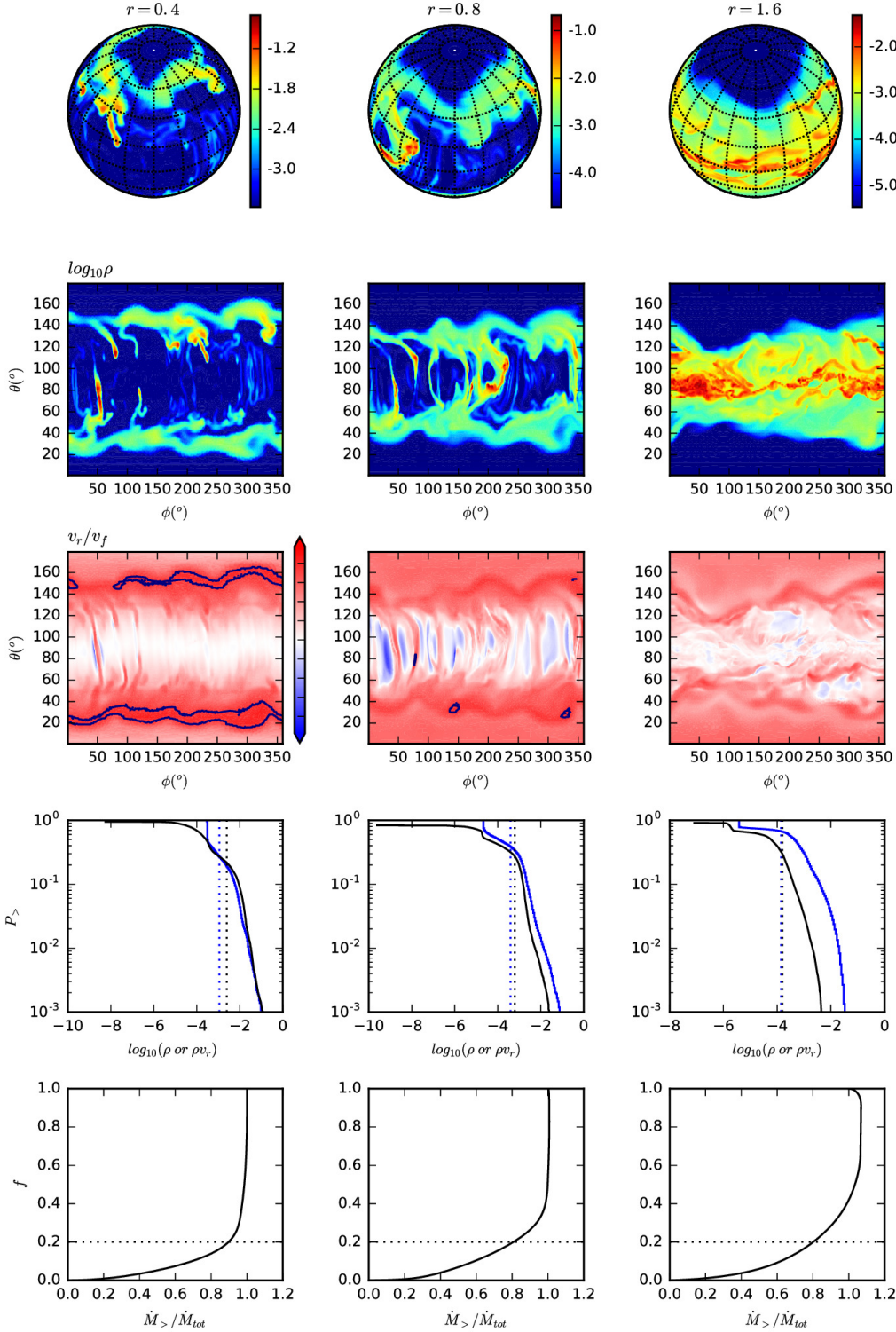


**Figure 14.** Various quantities at  $r = 0.4$ ,  $0.8$ , and  $1.6$  (left, middle, and right columns). The upper two rows show  $\log_{10}\rho$  mapped to a sphere (the top row) and in the  $\phi$ - $\theta$  plane (the second row). The third row shows the radial velocity normalized to the free-fall velocity at those three different radii. The colorbar extends from -1 to 1, and the black contour represents the value of 0.8. The fourth row shows the fraction of the area on the sphere with density ( $\rho$ , blue curves) or radial mass flux ( $\rho v_r$ , black curves) larger than the given value at x-axis. The vertical black and blue lines label where the radial mass flux and density should be for spherically symmetric accretion with the measured accretion rate (0.005) and the free-fall velocity. The bottom panels show the fraction of the sphere ( $f$ ) where the integrated accretion rate is  $\dot{M}_{>}$ . To derive  $\dot{M}_{>}$ , we integrate the mass flux from the highest flux region to the lowest flux region.



tosphere ( $r=0.4$  and  $0.8$  panels). The  $r=0.4$  panel suggests that most material will eventually fall onto the star at  $\theta \sim 30^\circ$  and  $150^\circ$ . We caution that the position of the hot spot also depends on the tilt of the dipole fields and/or the multipole field components (Long et al. 2008). Our discussion here is based on our simulation with the aligned dipole fields.

Figure 14 also shows that the filamentary features stretch from north to south, and fewer filaments penetrate into  $r = 0.4$  at the midplane compared with filaments at  $r = 0.8$ . The infalling material also accelerates as it falls, reaching free fall speed at  $r \sim 0.4$ . As discussed in Section 4.1, Figure 6 shows that the infall speed at moderate latitudes is almost the free-fall speed. We notice that there is more than one accretion hot spot and column, also shown in Figure 2. There could be many layers of magnetosphere with an onion-like structure. Recent observations by Thanathibodee et al. (2019b) find that some systems do have multiple geometrically isolated accretion flows, which seems to be consistent with our simulation.

Considering that accretion is concentrated at high altitudes and within several accretion columns, we calculate the fraction of the sphere where most accretion occurs (the ‘‘filling’’ factor). The fourth row in Figure 14 shows the fraction of the area with density ( $\rho$ ) or radial mass flux ( $\rho v_r$ ) higher than a given value. The vertical dotted lines label the density and radial mass flux for spherically symmetric accretion (labeled as  $\rho_{sph}$  and  $\rho_{sph} v_{ff}$ ) that is calculated using the measured accretion rate (0.005) and the free-fall velocity. At all three radii, roughly 30% of the area has a mass flux higher than  $\rho_{sph} v_{ff}$ . On the other hand, the density of the accretion columns in the outer disc is significantly higher than the  $\rho_{sph}$ , since the radial velocity there is significantly lower than the free-fall velocity. At  $r = 1.6$ , 70% of the area has a density higher than  $\rho_{sph}$ .

One important parameter in the magnetospheric accretion model is the filling factor,  $f$  (Hartmann et al. 2016) defined as the surface covering fraction of the accretion columns. With a small  $f$ , most accretion occurs within a small patch on the stellar surface. Since all accretion energy is released in such a small region, a small  $f$  produces a high temperature hot spot. For young stars, this produces UV excess emission over the photospheric SED, a distinct feature indicating magnetospheric accretion. On the other hand,  $f$  is less well defined in our simulations, since accretion occurs across a wide range of densities and mass fluxes over the sphere, rather than in discrete patches. Thus, we define a filling factor function,  $f(\dot{M})$ , as the surface covering fraction for regions where the integrated mass flux is  $\dot{M}$ . We integrate the mass flux from the patch with the highest mass flux to the patch with the lowest mass flux. More specifically, to calculate this function, we first calculate the distribution function for  $M_r \equiv \rho v_r$  as the probability of finding accreting columns within a certain range

of  $M_r$  values across all  $4\pi$  direction at  $r$ ,

$$P(M_{r,1} < M_r < M_{r,2}) = \int_{M_{r,1}}^{M_{r,2}} P(M_r) dM_r, \quad (29)$$

where  $P$  is calculated by dividing the solid angle corresponding to the selected  $M_r$  range by the total solid angle of  $4\pi$  steradians. Essentially, we rearrange all patches on the stellar surface according to its mass flux. Then, we integrate  $P$  from the patch with the highest mass flux  $M_{r,max}$  all the way down to  $M_{r,\dot{M}}$  to derive  $f(\dot{M}_>)$ :

$$f(\dot{M}_>) = - \int_{M_{r,max}}^{M_{r,\dot{M}}} P(M_r) dM_r, \quad (30)$$

where  $\dot{M}_>$  is the integrated flux for top accreting patches

$$\dot{M}_> = \int_{M_{r,max}}^{M_{r,\dot{M}}} \rho v_r P(M_r) 4\pi r^2 dM_r. \quad (31)$$

The filling factor  $f(\dot{M}_>)$  is shown in the bottom panels of Figure 14. From the right to left panels, the filling factor is smaller at the inner radius. At  $r = 0.8$ , 90% of the accretion occurs within 30% of the area. At  $r = 0.4$ , 90% of accretion occurs within 20% of the area, and 50% of accretion is within 5% of the area. Thus, we estimate that the filling factor is  $\sim 5\%$ -20%. We caution that, at smaller radii, the filling factor could be even smaller.

Since most accretion is concentrated in a few accretion columns and these columns appear and disappear dynamically due to the interchange instability, it is natural to ask if such an accretion is steady. We integrate the total accretion rate over the sphere at  $r = 0.4, 0.8$ , and  $1.5$  respectively, and plot the accretion rates with respect to time in the top panel of Figure 15. The accretion rates at all three radii are almost the same, indicating a constant accretion rate from the disc to the star. There is little time lag among the accretion rates at all three radii, even when the accretion rate changes by a factor of 2 over  $\sim 10$  orbits at the beginning of the simulation. This simultaneous change of the accretion rates at all three radii is due to the fast radial inflow from the disc surface accretion and magnetospheric accretion.

After 30 orbits, the accretion rates become almost constant. From the insert of Figure 15, it is evident that the accretion rate in the disc (e.g.  $r = 1.5$ ) is smoother than those in the magnetosphere (e.g.  $r = 0.4$  and  $r = 0.8$ ). These short time-scale fluctuations within the magnetosphere are probably due to the filaments produced by the interchange instability. On the other hand, the amplitudes of the  $\dot{M}$  variability are similar at these three radii, as shown in Figure 16. The averaged rates are within 15% of each other and the ratio between the standard deviation of the accretion rates and the mean accretion rates is also close to each other ( $\delta\dot{M}/\langle\dot{M}\rangle \sim 23\%$ ). This relatively steady accretion is consistent with TW Hya’s



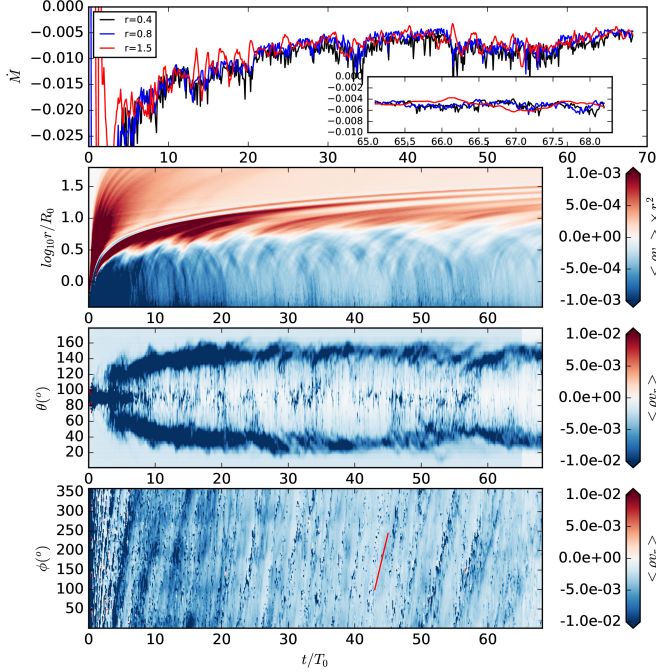


**Figure 15.** Top panel: evolution of the mass accretion rate at  $r = 0.4, 0.8,$  and  $1.5$  with time. The insert zooms into the last 3 orbits. The bottom three panels are space time diagram for  $\rho v_r$  along  $r, \theta,$  and  $\phi$  directions. The  $\dot{M}$  and  $\rho v_r$  in the top two panels are integrated and averaged over the sphere respectively. The  $\rho v_r$  in the  $t-\theta$  and  $t-\phi$  panels are averaged along the  $\phi$  and  $\theta$  directions at  $r = 0.4$ . The red line in the bottom panel shows the azimuthal movement for a hot spot if its orbital frequency is 20% of the Keplerian frequency at the magnetospheric truncation radius.

steady accretion over the past 20 years (Herczeg et al. 2023).

The  $\dot{M}$  distribution along the  $r, \theta,$  and  $\phi$  directions are shown in the spacetime plots in Figure 15. In the radial direction, there is a region of steady accretion which grows with time, beyond which there is a transition region that also moves outwards (with positive  $\rho v_r$ ). In the  $\theta$  direction, most accretion onto the star occurs around 30 and 150 degrees. The  $\phi$  panel shows that the accretion is not axisymmetric. This is expected due to the filaments within the magnetosphere. However, most interestingly, the accretion hot spot rotates around the central star at 20% of the Keplerian frequency at the magnetospheric truncation radius.

This  $5T_0$  periodicity is also shown in the periodogram for the accretion rate at one particular  $\phi$  angle. The bottom panel of Figure 17 shows that the periodogram for  $\phi = 0$  has a peak around  $5T_0$ . On the other hand, there are many other peaks due to the statistical noise. Thus, we averaged all the periodograms in different  $\phi$  directions to lower the noise, and the averaged curve is the red curve. We still see a bump around  $5T_0$ , confirming

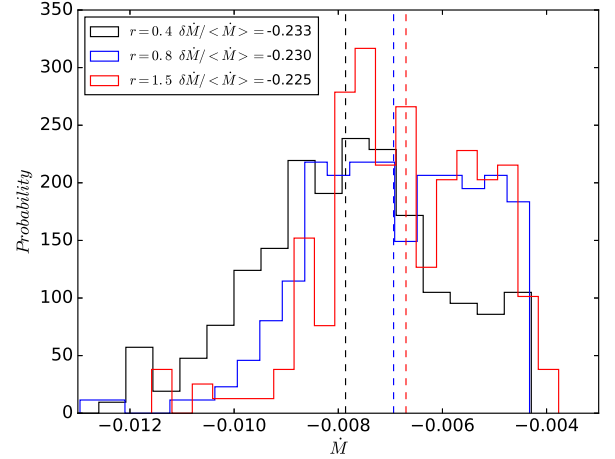


**Figure 16.** The probability distribution function of the accretion rates at  $r=0.4, 0.8,$  and  $1.5$  (black, blue, and red curves). They are derived using 341 snapshots uniformly spanned from half of the total time ( $t=34.1$ ) to the end of the simulation. The integration of the probability over all the  $\dot{M}$  is 1. The vertical lines are the averaged accretion rates. The standard deviation of the accretion rates is also given in the upper left corner.

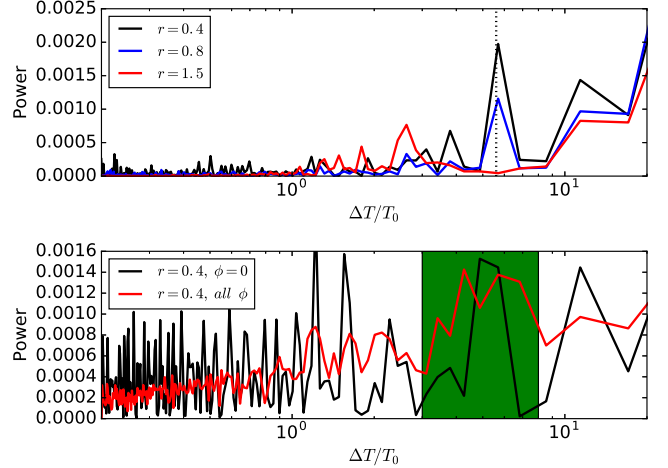


**Figure 17.** Top panel: the periodogram for the integrated mass accretion rate at  $r = 0.4, 0.8,$  and  $1.5$ . Bottom panel: the periodogram for the accretion rate at  $r = 0.4$  and  $\phi = 0$  (black curve) and the averaged curve of all the periodograms for the accretion rate at  $r = 0.4$  in 256  $\phi$  directions (red curve). The mass accretion rate data are from the top and bottom panels of Figure 15, and we use 341 snapshots from 34.1 to 68.2  $T_0$ . The red curve in the bottom panel has been stretched vertically by a factor of 1.5 to highlight its features.

the trend in the space-time diagram at the bottom panel of Figure 15. This  $5T_0$  modulation is linked to the orbital motion of the magnetic bubble in Section 4.3. The

middle panels in Figure 8 show that the magnetic bubble develops around  $R_T$  but it extends all the way to the central star. A dense filament can be seen at the edge of the bubble, connecting to the star. The filament is most apparent in the middle panels from 54 to 61  $T_0$  and this accreting filament can also be seen in the bottom panel of Figure 15 during the same period of time (the bubble and filament actually start around 50  $T_0$  shown in the movie after Figure 8). In terms of astronomical observations, we anticipate that such accretion modulation would be observable in inclined systems when the accretion hot spot undergoes orbital motion around the star at this particular frequency.

We have also calculated the periodogram for the integrated accretion rate over the sphere at  $r = 0.4, 0.8,$  and  $1.5$  (top panel of Figure 17). At both  $r = 0.4$  and  $0.8$ , there is also a peak at  $\sim 5.5 T_0$  which could also be related to the modulation and duration of the magnetic bubble. On the other hand, the power in the periodogram increases with  $\Delta T$ , and there could be more peaks at larger  $\Delta T$  which can only be studied with long timescale simulations.

### 5.2. The Spin-up Torque

The star is spun up by its coupling with the disc through magnetic fields. The total angular momentum of the star and the disc is conserved. If we integrate Equation 5 over the whole volume from  $r = r_{in}$  to  $r = r_{out}$ , we can derive the region's angular momentum change

$$\begin{aligned} \frac{\partial \int_{r_{in}}^{r_{out}} R \rho v_\phi dv}{\partial t} &= \int_{r_{in}} R_{in} (\rho v_r v_\phi - B_r B_\phi) dS \\ &\quad - \int_{r_{out}} R_{out} (\rho v_r v_\phi - B_r B_\phi) dS, \end{aligned} \quad (32)$$

where the first and second terms on the right-hand side are the integrals over the sphere at  $r_{in}$  and  $r_{out}$ . When the integrated stress at  $r$  is positive, the spherical region within it loses angular momentum. If the disc region extends from  $r_{in}$  to a very large  $r_{out}$  where the density and velocity are close to zero, the second integral on the right-hand side becomes zero. Since angular momentum can be changed by torque, the first term on the right-hand side can be considered as the torque between the disc and the star. The  $B_r B_\phi$  term is the magnetic stress/torque and the  $\rho v_r v_\phi$  term is the hydrodynamical stress/torque that includes both the turbulent stress/torque ( $\rho v_r \delta v_\phi$ ) and angular momentum carried by the accreting material ( $\rho v_r \langle v_\phi \rangle$ ). We integrate the total torque over the sphere at  $r = 0.4, 0.8,$  and  $1.5$ , and plot them with time in Figure 18. All three curves overlap with each other, suggesting that the disc has reached a constant angular momentum flow within  $r = 1.5$ . If we divide the torque by  $\dot{M}(GM_* R_T)^{1/2}$ , we derive the  $n$  parameter in Equation 9. The measured mean value of  $n$  is  $\sim 0.8$  with the standard deviation of

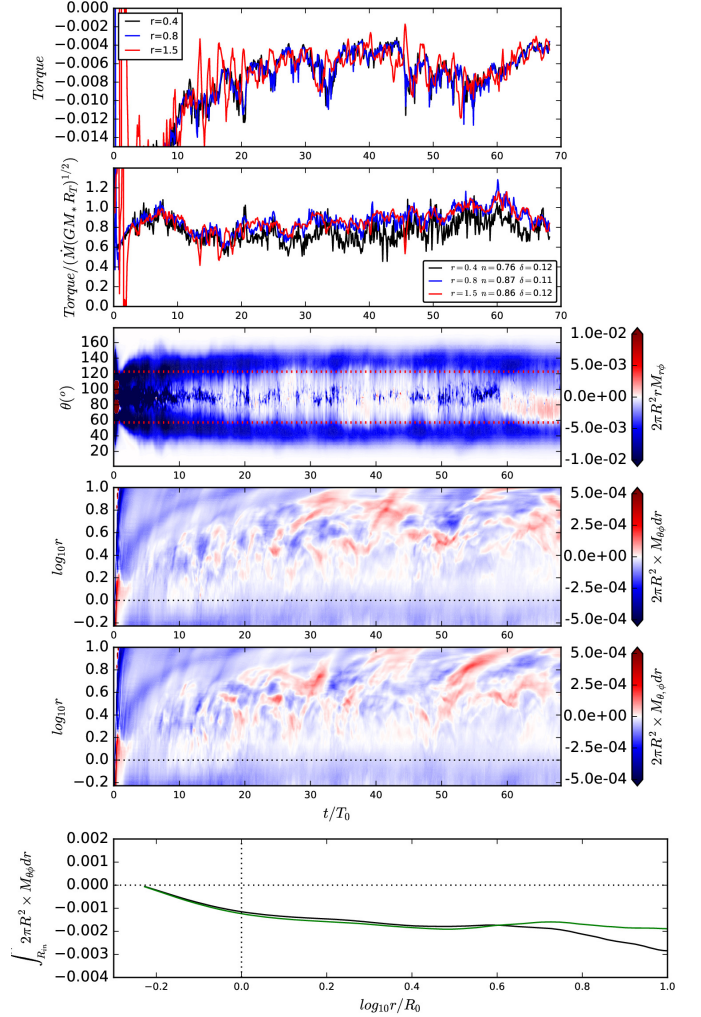


**Figure 18.** Top two panels: total torque and the  $n$  parameter at  $r=0.4, 0.8,$  and  $1.5$  with time. The average and the standard deviation of  $n$  after 10 orbits are given in the legend of the second panel. Third panel: the torque ( $\langle M_{r\phi} \rangle 2\pi r^3 \sin^2 \theta$ ) at  $r = 0.6$  along the  $\theta$  direction. Fourth and fifth panels:  $\langle M_{r\phi} \rangle 2\pi r^2 \sin^2 \theta \Delta r$  along the  $r$  direction at  $\theta=1$  and  $\pi-1$  ( $S_2$  and  $S_3$  areas in Figure 19). Bottom panel: integrated torques along  $S_2$  (black curve) and  $S_3$  (green curve) averaged from  $t = 50 T_0$  to the end of the simulation.

$\sim 0.1$ , shown in the second panel of Figure 18. The distribution of the torque along the  $\theta$  direction at  $r = 0.6$  is shown in the third panel of Figure 18. We can see that most of the torque is exerted at  $\theta \sim 45^\circ$  and  $135^\circ$ , corresponding to regions where the highest accretion rates are observed at  $r = 0.6$ .

The torque between the star and the disc sets the constant in Equation 10, and this constant is essential for the disc evolution. To understand how different stress/torque terms contribute to the total torque, we plot the Maxwell stress/torque and the hydrodynamical stress/torque in Figure 20. Close to the stel-

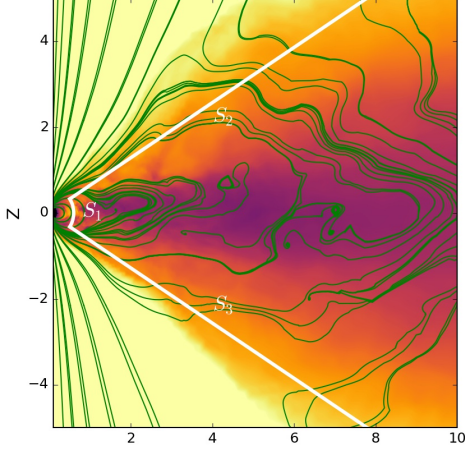


**Figure 19.** The azimuthally averaged density and poloidal magnetic streamlines at the end of the simulation. The white lines label the surfaces where the torques are calculated in Figure 18.

lar surface (e.g.  $r=0.4$ ), the magnetic stress dominates and is exerted at high latitudes where most of accretion occurs. This indicates that the accretion disc twists the magnetic fields that connect to the star, and these field lines torque the star while channeling the accretion flow. While the magnetic stress spins up the star (bottom panels), the small hydrodynamical stress actually tries to spin down the star (middle panels). This is because the infalling gas rotates in the opposite direction from the disc (§4.4) and the star thus accretes gas with negative angular momentum. Around the magnetospheric truncation radius (e.g.  $r=0.8$ ), the hydrodynamical stress from the penetrating filaments at the disc midplane becomes more apparent, while the total stress remains the same as the stress at  $r=0.4$ . At  $r=1.5$ , the magnetic stress is  $\sim 0$ , and the positive magnetic stress in the disc region is balanced by the negative magnetic stress higher above. This means that the hydrodynamical stress equals the constant. For the disc region (e.g.  $r=3$ ), both hydrodynamical and magnetic stresses become larger than the constant (see the discussion after Equation 10), and the magnetic stress drives the accretion inwards. The stress profiles along the radial direction is shown in Figure 21. Overall, the magnetic fields within the magnetosphere transfer angular momentum to the star, while the magnetic fields in the disc transfer angular momentum outwards. The magnetic stress changes sign at  $r \sim 1.5$ , slightly outside the magnetospheric truncation radius.

The fact that the  $n$  parameter is  $\sim 1$  suggests that most of the coupling between the magnetosphere and the disc occurs around  $R \sim R_T$ . To confirm this and understand how different disc regions contribute to the star’s spin-up, we calculate the stress at the interface between the disc region and the magnetosphere, shown as  $S_1$ ,  $S_2$ , and  $S_3$  in Figure 19. The total torque in the

disc region can be separated into

$$\begin{aligned} \frac{\partial \int R \rho v_\phi dv}{\partial t} &= \int_{S_1} R_{in} (\rho v_r v_\phi - B_r B_\phi) dS \\ &+ \int_{S_2} R (\rho v_\theta v_\phi - B_\theta B_\phi) dS \\ &- \int_{S_3} R (\rho v_\theta v_\phi - B_\theta B_\phi) dS, \quad (33) \end{aligned}$$

where  $S_1$  is the shell from  $\theta = 1$  to  $\pi - 1$  at  $r_{in} = 0.6$ , while  $S_2$  and  $S_3$  are surfaces of a cone at  $\theta = 1$  and  $\theta = \pi - 1$  from  $r_{in} = 0.6$  outwards.  $S_2$  and  $S_3$  are chosen to enclose the disc region, including the surface accretion region. The space-time diagrams for these three terms are shown in the third to fifth panels of Figure 18. Since most of the torque at  $r = 0.6$  is exerted beyond the  $\theta = [1, \pi - 1]$  region (the third panel), the integrated torque at  $S_1$  is small compared with the torque at  $S_2$  and  $S_3$ . The fourth and fifth panels show that most of the torque at  $S_2$  and  $S_3$  is from the region within  $r \sim 1$ . The white band extending from  $\log_{10} r \sim 0$  to  $0.4$  suggests that the torque density is  $\sim 0$  beyond  $r \sim 1$ . This is also confirmed in the bottom panel showing the integrated torques at  $S_2$  and  $S_3$ . The total torque averaged over the last 50  $T_0$  is  $-0.0065$ , and the torque at  $S_1$  during the same period of time is  $-0.0020$ . The bottom panel shows that the torques at  $S_2$  and  $S_3$  are also  $\sim -0.0020$ . At  $r = 1$ , the integrated torques at  $S_2$  and  $S_3$  are both  $-0.0012$ . Thus, 70% of the total torque is exerted at the disc surface within  $r = 1$ , and 90% of the torque is exerted within  $r = 3$ .

Our torque results are noticeably different from recent work by Takasao et al. (2022) who finds significant hydrodynamical stress contribution close to the star and the  $n$  parameter is significantly smaller than 1. Especially for their model C, whose large corotation radius is similar to our non-rotator setup, its  $n$  value is  $\sim 0$ . Two factors could contribute to the difference. The first is that our truncation radius is 10 times the stellar radius while their truncation radius is 2 times the stellar radius due to their much weaker stellar field. As shown in Figure 20, magnetic stress is more important deeper into the magnetosphere. The second difference is the strong outflow in Takasao et al. (2022), which is absent in our simulations. The difference in the outflow rate could be due to the disc fields applied in Takasao et al. (2022) the different adopted coronal density/density floor around the star. The impact of the coronal density/density floor is an important issue which needs to be thoroughly examined in future.

### 5.3. Field Transport

The transport of net magnetic flux in discs directly controls the disc’s long-term evolution. However, studying magnetic field transport in discs can be challenging, often influenced by inner boundary conditions of the



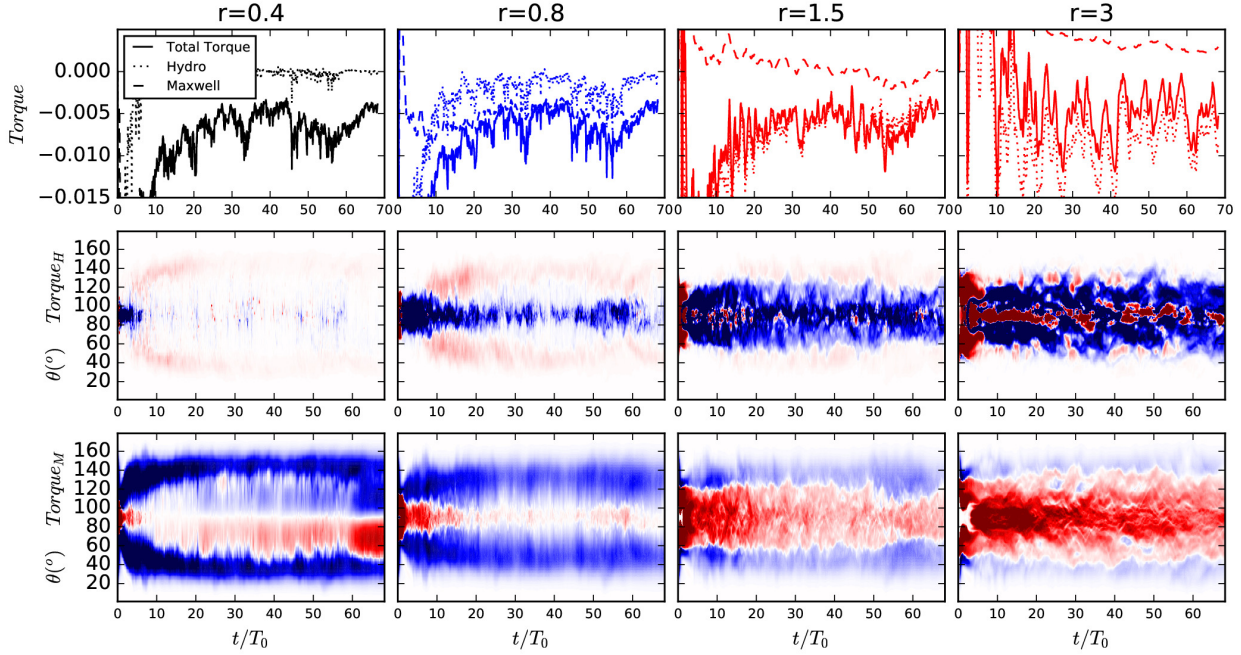


**Figure 20.** Similar to Figure 18 but for different stress components. Top panels: the integrated torque over spheres at different radii (left to right panels) with time. The middle and bottom panels: the hydrodynamical and magnetic components of the torque along the  $\theta$  direction with time. The normalization and colorbar are the same as those in the third panel in Figure 18.

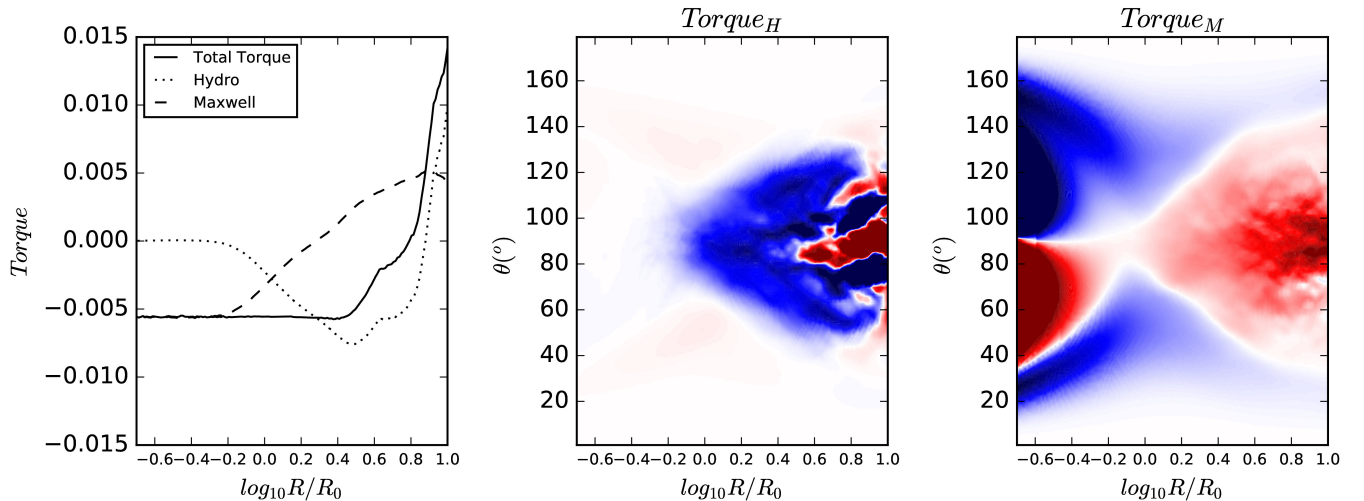


**Figure 21.** The left panel: the integrated torque over spheres at different radii. The middle and right panels: the hydrodynamical and magnetic components of the torque along the  $\theta$  direction with radii. The normalization and colorbar are the same as those in the third panel in Figure 18. The torques have been averaged using 100 snapshots over the last 10 orbits.

simulation. Fortunately, our simulation setup has two advantages allowing us to study field transport. First, our setup incorporates the central star within the simulation domain, and the stellar magnetic fields are the only source of magnetic fields in the problem. Thus, there is no need for special boundary conditions at the stellar surface. Second, Athena++ conserves the total

magnetic flux in the whole domain to machine precision, except for flux losses at the boundaries.

To examine flux transport, we monitor the evolution of magnetic flux integrated outward from the central star. Given our Cartesian grid setup, we integrate the flux over the area of a circle at the disc midplane. The integrated flux within different sized circles around the central star is shown at the bottom panel of Figure 22.



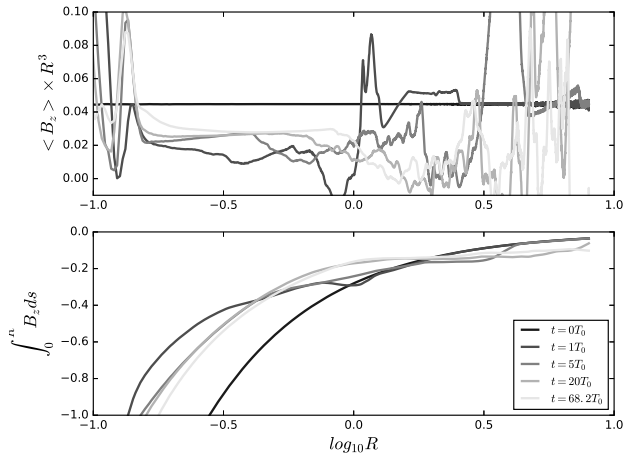


**Figure 22.** The azimuthally averaged vertical magnetic fields (upper panel) and the radially integrated magnetic flux (lower panel) at the midplane. Dark to light colored curves show  $t = 0, 1, 5, 20, 68.2 T_0$  respectively.

Shortly after the simulation starts, the dipole magnetic fields begin moving outward, reducing the dipole field strength within  $r \sim 1$ . This decrease of dipole fields is likely due to field inflation and the reconnection at the beginning of the simulation (Figure 13). The outward moving fields are piled up at the disc region (the high  $B_z$  values that are above the initial field strengths in the upper panel of Figure 22). With outer regions becoming MRI active, the fields are transported further outwards. At the end of our simulation, the whole region within  $R \sim 5$  has weaker fields than the initial condition. The disc region beyond  $R \sim 1$  seems to have the most significant field reduction compared with the magnetosphere region within  $R \sim 1$ . Overall MRI turbulence in the disc seems to be efficient at transporting the fields outwards. The outward moving fields may accelerate the operation of MRI at the outer discs.

Such outward field transport is different from field transport in simulations with net vertical fields. Previous net vertical field simulations find that either the fields are transported to the star (Zhu & Stone 2018; Jacquemin-Ide et al. 2021) at the mass accretion timescale (Jacquemin-Ide et al. 2021) or maintains a quasi-steady state (Mishra et al. 2020). Such difference indicates that field transport also depends on the initial field distribution besides the accretion disc properties. To achieve a long-term equilibrium field configuration, it is necessary to conduct simulations that run for significantly longer timescales. The field transport could also be affected by non-ideal MHD effects at the outer disc or the multiple components of the fields (Russo & Thompson 2015).

#### 5.4. Implications for Planet Formation

Our simulation can be scaled to realistic astronomical systems that undergo magnetospheric accretion. When considering a disc that is threaded by the stellar dipole fields and it has the same temperature slope ( $q = -1/2$  in Equation 18) as in our simulation, there are only two dimensionless free parameters to define the system: the disc aspect ratio at the magnetospheric truncation radius ( $h(R_T)$ ), and the ratio between  $R_T$  and  $R_*$ . Since material undergoes free fall toward the central star within the magnetosphere, the region immediately surrounding the star is unlikely to have a significant impact on the dynamics within the disc, except through thermal feedback. Thus, the only important free parameter is  $h(R_T)$ . Although we have only studied the thick disc case with  $h(R_T) = 0.1$  here, we will explore thinner discs, which will be more applicable to protoplanetary discs, in future works. Nevertheless, we still use our current simulation results to study protoplanetary discs and will justify some parameter choices later.

We consider a typical protoplanetary disc with an accretion rate of  $\dot{M} = 10^{-8} M_\odot \text{ yr}^{-1}$  around a  $2 r_\odot$ ,  $0.5 M_\odot$  star having a 1kG dipole magnetic field. The magnetic truncation radius (Equation 8) is thus

$$R_T = 14.4 \left( \frac{B_*}{1kG} \right)^{4/7} \left( \frac{M_*}{0.5 M_\odot} \right)^{-1/7} \left( \frac{\dot{M}}{10^{-8} M_\odot \text{ yr}^{-1}} \right)^{-2/7} \left( \frac{r_*}{2 r_\odot} \right)^{12/7} r_\odot. \quad (34)$$

$R_T/r_* = 7.2$  which is quite close to our  $R_T/r_* = 10$  in the simulation<sup>3</sup>. To represent this fiducial system, the length unit in our simulation  $R_0$  is  $14.4 r_\odot$  or  $0.067 \text{ au}$  since  $R_0 \sim R_T$ . The time unit ( $1/\Omega_0$ ) is thus  $0.0039$  years. If we equate  $\dot{M} = -0.005$  in our code unit with  $\dot{M} = 10^{-8} M_\odot \text{ yr}^{-1}$ , the mass unit is  $7.8 \times 10^{-9} M_\odot$ . The surface density unit is then  $15.5 \text{ g/cm}^2$ . Thus, the disc surface density  $\sim 0.003 R$  from  $R = 1$  to  $R = 10$  (Figure 9) is equivalent to a protoplanetary disc with the surface density of

$$\Sigma = 0.7 \times (R/\text{au}) \text{ g/cm}^2 \quad \text{at } r < 0.7 \text{ au}. \quad (35)$$

The increase of  $\Sigma$  with  $R$  is due to the fast decrease of  $\alpha$  with  $R$ . With this surface density, the total gas mass within  $R$  is

$$M(R) = \int_0^R 2\pi R \Sigma dR = 0.055 (R/\text{au})^3 M_\oplus. \quad (36)$$

Assuming the dust-to-gas mass ratio is 1 to 100, the total dust mass is 100 times smaller. This low value of  $\Sigma$  is caused by the large  $\alpha$  value within the disc resulting

<sup>3</sup> For a star with weaker magnetic fields,  $r_*/R_T$  is larger. To scale our simulation for such a star, we could assume that the stellar surface is at the given  $r_*/R_T$  in the current simulation.

from surface accretion. Figure 9 shows that  $\alpha_{int} \sim 1$  at  $R \sim 3$ , which is scaled to

$$\alpha_{int} \sim 0.1 \times (R/au)^{-1.5}, \quad (37)$$

in the MRI active region of the protoplanetary disc. Using  $\dot{M} = 3\pi\nu\Sigma$ , we can estimate that  $\Sigma \sim 2 \text{ g/cm}^2$  at  $R \sim 0.2 \text{ au}$  assuming a more realistic  $h/r \sim 0.05$ . This surface density is  $\sim 10$  times larger than Equation 35. But even so, the mass is orders of magnitude smaller than what would be required to explain the discovered exoplanets within 1 au. Furthermore, dust may evaporate in this region. Thus, exoplanets may not be able to form in the MRI active inner disc. On the other hand, they could form at the inner edge of the dead-zone and later migrate inwards. Dust growth in this inner disc region is crucial for both planet formation and explaining dipper stars (Li, Chen, & Lin 2022).

To estimate the location of the inner edge of the dead zone, it's necessary to calculate the temperature distribution within the disc. MRI becomes active when the disc temperature exceeds  $\sim 1000 \text{ K}$ . An accurate estimate requires us to know how accretion energy is dissipated in the disc. Since we have little knowledge on this, we simply estimate the lower limit of the disc temperature using the irradiation equilibrium temperature. Assuming that the disc absorbs a fraction ( $\epsilon$ ) of the total stellar luminosity ( $L_*$ ), the equilibrium temperature is then

$$T_{irr} = 394 \left(\frac{R}{au}\right)^{-1/2} \left(\frac{\epsilon L_*}{L_\odot}\right)^{1/4} K. \quad (38)$$

Since MRI becomes active when  $T \gtrsim 1000 \text{ K}$ , the inner edge of the deadzone is  $0.07 \text{ au}$  if  $\epsilon L_* = 0.2 L_\odot$ . On the other hand, if viscous heating is included, the inner deadzone edge can be  $0.2 \text{ au}$  (D'Alessio et al. 1998). For Herbig Ae-Be stars, this radius can be even larger, reaching to  $1 \text{ au}$  (Dullemond & Monnier 2010). Within this radius where the disc couples efficiently with the stellar magnetic fields and maintains a low surface density, the formation of the exoplanets within  $0.1 \text{ au}$  (10 day period) through in-situ formation is challenging. Instead, these exoplanets are likely to form at the outer discs and migrate inwards.

We can estimate the planet migration timescale in the MRI active disc using the derived disc surface density in Equation 35. The type I migration timescale (Baruteau et al. 2014) for a planet around a  $0.5 M_\odot$  star is then

$$\begin{aligned} t_{I,mig} &= \Omega^{-1} h^2 q^{-1} \left(\frac{\Sigma R^2}{M_*}\right)^{-1} \\ &= 1.1 \times 10^{10} \left(\frac{R}{0.1 \text{ au}}\right)^{-1.5} \left(\frac{q}{10^{-5}}\right)^{-1} \left(\frac{h}{0.05}\right)^2 \text{ yr}, \end{aligned} \quad (39)$$

where  $q \equiv M_p/M_*$ . When this mass ratio is higher than  $\alpha^{1/2} h^{5/2}$  (Zhu et al. 2013), a gap will be induced in the

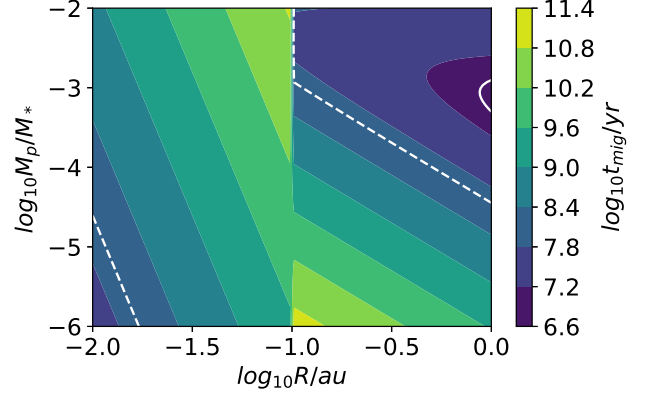


**Figure 23.** The migration timescale for a planet at the inner disc. We assume that the magnetospheric truncation radius is at  $0.1 \text{ au}$ . Outside this radius, disc-driven migration (Equation 41) is important. We adopt the disc's surface density from Equation 35,  $h = 0.05$ , and  $\alpha$  from Equation 37. Within  $0.1 \text{ au}$ , aerodynamic drag is important (Equation 43). The solid and dashed white contours label the migration timescale of  $10^7$  and  $10^8$  years. The central star is a  $0.5 M_\odot$  star.

disc and the planet undergoes Type II migration. The Type II migration rate is (Ivanov et al. 1999; Dempsey et al. 2020)

$$t_{II,mig} = \tau_{visc} \frac{M_p}{\Sigma R^2} = \Omega^{-1} h^{-2} \alpha^{-1} q \left(\frac{\Sigma R^2}{M_*}\right)^{-1}. \quad (40)$$

We could combine both Type I and Type II migration rates (Equations 39, 40), and incorporate the effects of the gap-opening planet mass into a single equation that represents the overall planet migration rate

$$t_{mig} = \Omega^{-1} h^2 q^{-1} \left(\frac{\Sigma R^2}{M_*}\right)^{-1} (1 + hK), \quad (41)$$

where  $K \equiv q^2/(\alpha h^5)$ . When  $K \lesssim 1/h$ , it reduces to the Type I rate, as shown in Figure 12 of Dempsey et al. (2020). Unlike Type I migration, the Type II migration timescale is longer for a more massive planet. Thus, a planet that can marginally induce gaps ( $hK \sim 1$ ) migrates fastest in the disc. With the high  $\alpha$  value in our simulations, Jupiter mass planets marginally induce gaps in the disc. Figure 23 shows the planet's migration timescale calculated with our disc structure from Equation 35. For this calculation, we ignore the fact that the planet will undergo stochastic migration due to MRI turbulence. The planet's stochastic migration in a disc that undergoes magnetospheric accretion will be presented in a future publication. Nevertheless, if we only consider Type I and Type II migration, the planet migration timescale is much longer than the disc's lifetime, except for giant planets at  $\sim 1 \text{ au}$ . Most planets cannot undergo disc migration within the inner MRI

active disc, except early times when the disc’s accretion rate and surface density is a lot higher. Planets are likely to stall or become trapped at the inner edge of the deadzone. Thus, it is the inner deadzone edge, instead of the magnetospheric truncation radius, that determines the planet’s final position before the protoplanetary disc dissipates. This could have important implications for the distribution of exoplanets.

On the other hand, if a planet manages to migrate through the inner MRI turbulent disc (via either disc migration or planet-planet scattering) and gets into the magnetosphere, the planet will be subject to strong aerodynamic drag which accelerates its migration to the central star. For a Keplerian orbiting object in a Keplerian rotating disc, the relative motion between the planet and the local disc flow is small, and the interactions between the planet and the disc are mostly through resonance interactions (e.g. Lindblad and Corotation resonances). However, if the relative motion between the planet and background flow becomes significant, dynamical friction and aerodynamic drag start to play a more important role. One example where these effects manifest is the interaction between an inclined planet and a Keplerian rotating disc (Rein 2012; Arzamasskiy et al. 2018). As the material in the magnetosphere corotates with the star, it rotates significantly slower than the Keplerian speed. In our simulation having a non-rotating star, the material inside the magnetosphere has nearly zero azimuthal velocity (Figure 6). Thus, the relative speed between the planet and the magnetosphere is the local Keplerian speed. As a result, the planet within the magnetosphere experiences strong head-wind and migrates inwards.

Although both aerodynamic drag and dynamical friction could be important when the relative motion between the object and the background flow is nonzero, aerodynamic drag plays a more important role for a planet in the magnetosphere. The ratio between the aerodynamic drag force and the dynamical friction force is roughly the square of the ratio between the object’s size and its Bondi radius ( $R_{Bondi} = GM_p/v_{rel}^2$ ) (e.g., Rein 2012; Wang et al. 2023). The Bondi radius, for a planet that is within 10 solar radius distance to the star, is at least one order of magnitude smaller than the planet size assuming  $v_{rel} \sim v_K$ . If we only consider the aerodynamic drag force

$$\mathbf{f}_{aero} = -\pi s_p^2 \rho v_{rel} \mathbf{v}_{rel}, \quad (42)$$

where  $s_p$  is the planet’s radius, we can estimate the migration timescale

$$t_{mig} = \frac{M_p v_{rel}}{f_{aero}} = \frac{4s_p \rho_p}{3v_{rel} \rho}, \quad (43)$$

where  $\rho_p$  is the material density of the planet. The background density within the magnetosphere can be estimated by assuming that the accretion is from the

spherical infall at the free-fall speed

$$\rho = \frac{\dot{M}}{4\pi R^2 v_{ff}}. \quad (44)$$

We verify that, at a distance of 5 stellar radii, this density is only a factor of 2 smaller than the midplane density found in our simulation. The presence of intruding filaments resulting from interchange instability ensures that the gas density at the midplane within the magnetosphere remains non-negligible and approaches values estimated from the spherical infall. Our simulation here ignores the coronal heating within the magnetosphere which will change the temperature and density within the magnetosphere. However, the aerodynamic drag is mainly determined by the density, which is estimated from the mass conservation (Equation 44) and less affected by the coronal heating. Again, using the typical stellar parameters and the disc accretion rate as before, we calculate this timescale within 0.1 au, shown in Figure 23. The dashed contours label the parameter space for planets with a migration timescale of  $10^8$  years. Since both the disc-driven and aerodynamic-driven migration timescales are inversely proportional to the disc’s surface density, these contours can also be interpreted as the parameter space of planets with a migration timescale of  $10^7$  years in a  $\dot{M} = 10^{-7} M_\odot \text{yr}^{-1}$  disc.

Although the aerodynamic drag seems to accelerate the planet’s migration within the magnetosphere, the migration timescale is still longer than the disc’s lifetime for most parameter spaces. Thus, we would expect that any planet that ends in this region will stay in this region. However, their orbital configurations (e.g. eccentricity and inclination) might evolve due to the planet-disc or planet-magnetosphere interactions. Finally, we caution that we have ignored any electromagnetic effect (including dipole-dipole and dipole-conductor interactions, Bromley & Kenyon 2022) on the planet migration.

## 6. CONCLUSION

We have carried out high-resolution long-timescale MHD simulations to study magnetospheric accretion onto a non-rotating star. Adopting a Cartesian grid with mesh-refinement allows us to resolve both the disc and the polar accretion region equally well and reduces the computational cost significantly. We run the simulation for 68 orbits at the magnetospheric truncation radius ( $R_T$ ), which is equivalent to 2157 Keplerian orbits at the stellar surface. A steady accretion is reached within  $R \sim 6 R_T$ .

Figure 24 summarizes some of our key results. Surrounding the star, the flow within the magnetosphere is highly dynamic and filamentary. Within the magnetospheric truncation radius  $R_T$ , the filamentary flow is in the force-free limit, moving along the magnetic field lines. The formation of these filamentary structures is driven by the interchange instability at  $R_T$  where the



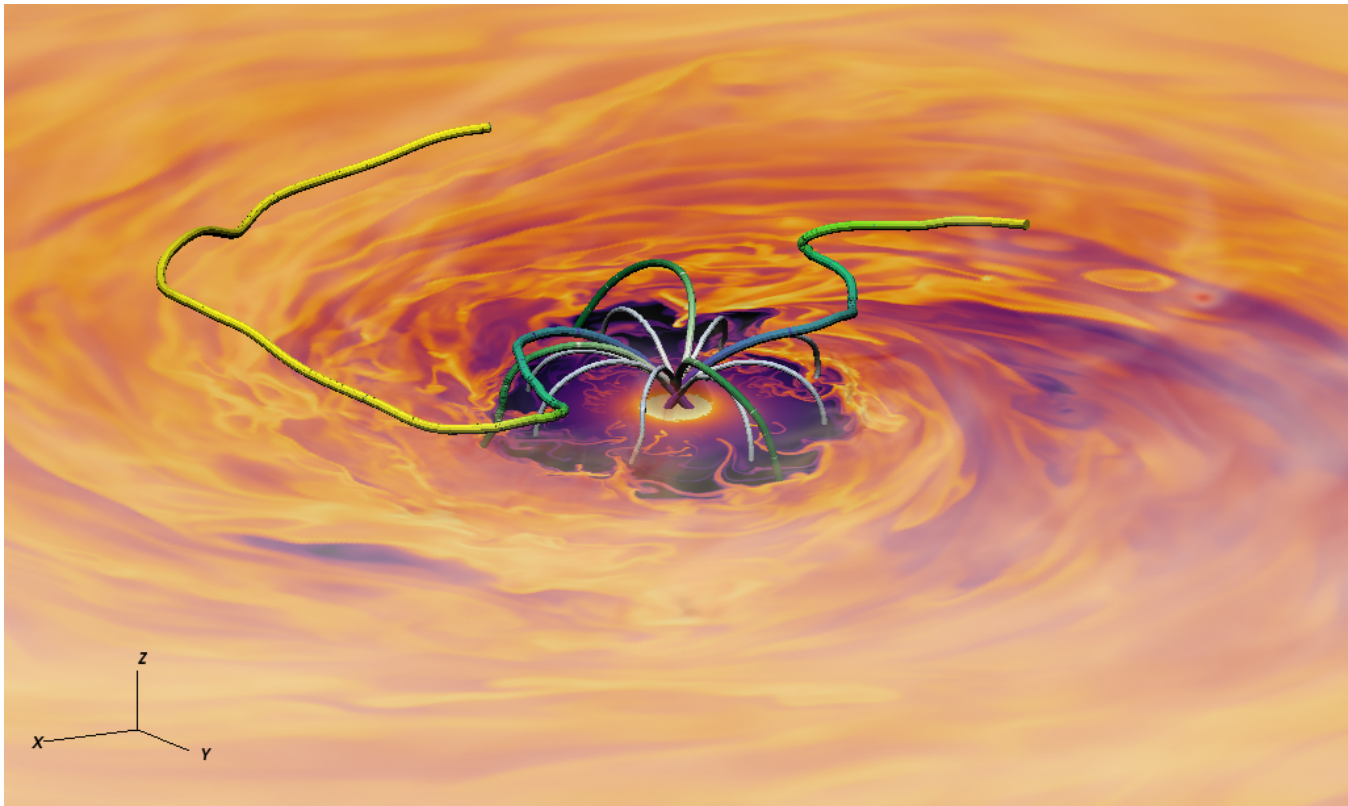


**Figure 24.** The color contours for density at the disc midplane, and the magnetic field lines within the magnetosphere and the disc.

density increases with radial distance. The developed filaments (“fingers”) could penetrate deep into the magnetosphere. The density within the filaments could be more than 3 orders of magnitude higher than the background density. As these filaments move in, they are lifted from the midplane and move along the dipole magnetic field lines. Eventually, most material accretes at  $30^\circ$  from the magnetic poles and falls to the star at close to the free-fall speed. More than 50% (90%) of accretion occurs within accretion columns covering 5% (20%) of the stellar surface area. Thus, we consider the filling factor to be  $\sim 5\text{-}20\%$ . Multiple accretion columns could develop simultaneously, forming an onion like structure with multiple isolated layers. Despite the filamentary structures, the total accretion rate onto the star is relatively steady with 23% standard deviation. Material falling onto the star has negative azimuthal velocity, since it follows the stellar magnetic field lines that are pitched forward by disc dragging. The stress from the magnetic fields spins up the star. The ratio between the spin-up torque and  $\dot{M}(GM_*R_T)^{1/2}$  is  $\sim 0.8$ , independent of the long-term accretion rate change. This constant torque will affect the disc’s long term evolution.

Many properties of the simulated flow within the magnetosphere are consistent with observations, including hot spots at high altitudes, free-fall velocities, low filling factors, and multiple accretion lay-

ers. On the other hand, recent observations by [Thanathibodee et al. \(2023\)](#) find that low accretors with  $\dot{M} < 2 \times 10^{-10} M_\odot \text{ yr}^{-1}$  have magnetospheres with sizes  $\sim 2 - 5 R_*$ , which is significantly smaller than the theory prediction ( $\sim 7 R_*$  from Equation 34). Possible explanations include a weaker dipole magnetic field ([Long et al. 2008](#)), a quadrupole/multipole magnetic field, or a more complicated thermal structure of the magnetosphere. Future theoretical and observational studies in these directions are desired.

Outside the magnetosphere, we have the highly magnetized disc. Although, at the disc midplane, the transition radius between the magnetosphere and the disc agrees well with the traditional magnetospheric truncation radius, these two regions are less distinct above the midplane. The disc surface accretion smoothly joins the magnetospheric accretion. If we use the Alfvén surface or the  $E_k/E_m \sim 1$  surface to separate these two regions, the transition radius becomes larger when it is higher up in the disc. The azimuthal velocity and azimuthal magnetic field also reverse their signs at the transition radius.

The disc region outside  $R_T$  is also highly variable due to the strong net vertical magnetic fields. Magnetic reconnection and interchange instability could occasionally reorganize magnetic fields around the truncation radius, leading to a large-scale density void that orbits around the central star at sub-Keplerian speed, similar

to the structures in MADs around blackholes. It takes  $\sim 5 T_0$  for the density void to finish one orbit. The density void extends all the way to the stellar surface, leading to hot spots that orbit at the same frequency as the void. The periodogram of disc accretion also shows a peak at  $\sim 20\%$  of the Keplerian frequency at  $R_T$ , which corresponds to the orbital motion of the hot spot and the lifetime of the bubble. We have also observed outflows that originate from the bubble. But the mass loss rate is quite low. Overall, both smaller-scale filaments and larger-scale magnetic bubbles are characteristics of a disc that is magnetically disrupted by strong fields.

Further away into the disc, a magnetically supported surface region plays a crucial role in disc accretion, which is distinctly different from the traditional model. Keplerian differential rotation stretches the radial component of the dipole magnetic fields to generate strong azimuthal fields, which lead to a low-density region up to  $z \sim R$ . The resulting strong  $R - \phi$  stress makes this surface region accrete inwards at supersonic speeds, which is similar to the surface accretion of an accretion disc with net vertical magnetic fields. However, little disc wind is launched above this region, since the magnetic fields there are connected to the non-rotating star instead of the Keplerian rotating disc. Both the net vertical magnetic fields and the disc  $\alpha$  decrease sharply with radii, which leads to a disc with a surface density proportional to  $R$  within  $R \sim 10R_T$ .

Our disc structure is significantly different from previous ‘‘X-wind model’’ (Shu et al. 1994) and the unsteady field inflation model (Lynden-Bell & Boily 1994; Lovelace et al. 1995; Uzdensky et al. 2002), which are built upon  $R$ - $z$  2-D models. During the early stage in the simulation when the disc is largely axisymmetric, we

observe strong field inflation as in previous works. However, when various 3-D instabilities start to operate, including the magnetic interchange instability around  $R_T$  and the MRI in the outer disc, the field lines diffuse across disc material, acting like a large anomalous resistivity. Thus, open field lines return to the dipole configuration due to the anomalous resistivity. With a large resistivity, the slippage of field lines balances the azimuthal shear, allowing the quasi-steady accretion.

After scaling our simulations to protostars with  $\dot{M} = 10^{-8} M_\odot \text{ yr}^{-1}$ , we find that the inner MRI active disc has a very low surface density ( $< 1 \text{ g cm}^{-2}$ ) due to the efficient surface accretion. The timescale for Type-I/II planet migration is longer than the disc lifetime, suggesting that planets (especially low mass planets) are not able to migrate in the inner MRI active region and likely to be stalled at the inner edge of the deadzone. If the planets could move into the magnetosphere, aerodynamic drag can accelerate the planet’s migration, although the migration timescale is still long.

#### ACKNOWLEDGEMENTS

All simulations are carried out using with NASA Pleiades supercomputer. Z. Z. acknowledges support from NASA award 80NSSC22K1413. J.M.S. acknowledges support from the Schmidt Futures Fund to the IAS. ZZ thanks Bart Ripperda, Catherine Dougados, Dong Lai, Yihan Wang, Douglas N.C. Lin for discussions and suggestions.

#### DATA AVAILABILITY

The data underlying this article will be shared on reasonable request to the corresponding author.

#### REFERENCES

- Aly, J. J., & Kuijpers, J. 1990, *A&A*, 227, 473
- Aoyama, Y., Ikoma, M., & Tanigawa, T. 2018, *ApJ*, 866, 84
- Arons, J., & Barnard, J. J. 1986, *ApJ*, 302, 120
- Arons, J., & Lea, S. M. 1976, *ApJ*, 207, 914
- Arzamasskiy, L., Zhu, Z., & Stone, J. M. 2018, *MNRAS*, 475, 3201
- Baruteau, C., Crida, A., Paardekooper, S. J., et al. 2014, in *Protostars and Planets VI*, ed. H. Beuther, R. S. Klessen, C. P. Dullemond, & T. Henning, 667–689
- Beckwith, K., Hawley, J. F., & Krolik, J. H. 2009, *ApJ*, 707, 428
- Begelman, M. C., & Armitage, P. J. 2023, *MNRAS*, 521, 5952
- Bessolaz, N., Zanni, C., Ferreira, J., Keppens, R., & Bouvier, J. 2008, *A&A*, 478, 155
- Bildsten, L., Chakrabarty, D., Chiu, J., et al. 1997, *ApJS*, 113, 367
- Blandford, R. D., & Payne, D. G. 1982, *MNRAS*, 199, 883
- Blinova, A. A., Romanova, M. M., & Lovelace, R. V. E. 2016, *MNRAS*, 459, 2354
- Bonnell, I. A., Smith, K. W., Meyer, M. R., et al. 1998, *MNRAS*, 299, 1013
- Bromley, B. C., & Kenyon, S. J. 2022, *AJ*, 164, 229
- Calvet, N., & Gullbring, E. 1998, *ApJ*, 509, 802
- Casse, F., & Ferreira, J. 2000, *A&A*, 353, 1115
- D’Alessio, P., Cantö, J., Calvet, N., & Lizano, S. 1998, *ApJ*, 500, 411
- Dempsey, A. M., Lee, W.-K., & Lithwick, Y. 2020, *ApJ*, 891, 108
- Dullemond, C. P., & Monnier, J. D. 2010, *ARA&A*, 48, 205
- Espaillet, C. C., Herczeg, G. J., Thanathibodee, T., et al. 2022, *AJ*, 163, 114
- Fender, R., Wu, K., Johnston, H., et al. 2004, *Nature*, 427, 222

- Fendt, C., & Elstner, D. 2000, *A&A*, 363, 208
- Ferreira, J., & Pelletier, G. 1995, *A&A*, 295, 807
- Ferreira, J., Pelletier, G., & Appl, S. 2000, *MNRAS*, 312, 387
- Gardiner, T. A., & Stone, J. M. 2008, *Journal of Computational Physics*, 227, 4123
- Ghosh, P., & Lamb, F. K. 1979a, *ApJ*, 232, 259
- . 1979b, *ApJ*, 234, 296
- Ghosh, P., Lamb, F. K., & Pethick, C. J. 1977, *ApJ*, 217, 578
- Goodson, A. P., Winglee, R. M., & Böhm, K.-H. 1997, *ApJ*, 489, 199
- Haffert, S. Y., Bohn, A. J., de Boer, J., et al. 2019, *Nature Astronomy*, 3, 749
- Hartigan, P., Edwards, S., & Ghandour, L. 1995, *ApJ*, 452, 736
- Hartmann, L., Herczeg, G., & Calvet, N. 2016, *ARA&A*, 54, 135
- Hartmann, L., Hewett, R., & Calvet, N. 1994, *ApJ*, 426, 669
- Hartmann, L., & MacGregor, K. B. 1980, *ApJ*, 242, 260
- Hayashi, M. R., Shibata, K., & Matsumoto, R. 1996, *ApJL*, 468, L37
- Herczeg, G. J., Chen, Y., Donati, J.-F., et al. 2023, *ApJ*, 956, 102
- Igumenshchev, I. V., Narayan, R., & Abramowicz, M. A. 2003, *ApJ*, 592, 1042
- Ingleby, L., Calvet, N., Bergin, E., et al. 2011, *ApJ*, 743, 105
- Ivanov, P. B., Papaloizou, J. C. B., & Polnarev, A. G. 1999, *MNRAS*, 307, 79
- Jacquemin-Ide, J., Lesur, G., & Ferreira, J. 2021, *A&A*, 647, A192
- Johnstone, C. P., Jardine, M., Gregory, S. G., Donati, J. F., & Hussain, G. 2014, *MNRAS*, 437, 3202
- King, A., Lasota, J.-P., & Middleton, M. 2023, *NewAR*, 96, 101672
- Kruskal, M., & Schwarzschild, M. 1954, *Proceedings of the Royal Society of London Series A*, 223, 348
- Kulkarni, A. K., & Romanova, M. M. 2008, *MNRAS*, 386, 673
- . 2013, *MNRAS*, 433, 3048
- Kurosawa, R., Romanova, M. M., & Harries, T. J. 2011, *MNRAS*, 416, 2623
- Lai, D. 2014, in *European Physical Journal Web of Conferences*, Vol. 64, *European Physical Journal Web of Conferences*, 01001
- Lamb, F. K., Pethick, C. J., & Pines, D. 1973, *ApJ*, 184, 271
- Lee, E. J., & Chiang, E. 2017, *ApJ*, 842, 40
- Lewin, W. H. G., & van der Klis, M. 2006, *Compact Stellar X-ray Sources*, Vol. 39
- Li R., Chen Y.-X., Lin D. N. C., 2022, *MNRAS*, 510, 5246
- Liu, B., Ormel, C. W., & Lin, D. N. C. 2017, *A&A*, 601, A15
- Long, M., Romanova, M. M., & Lovelace, R. V. E. 2008, *MNRAS*, 386, 1274
- Lovelace, R. V. E., Romanova, M. M., & Bisnovatyi-Kogan, G. S. 1995, *MNRAS*, 275, 244
- . 1999, *ApJ*, 514, 368
- Lynden-Bell, D., & Boily, C. 1994, *MNRAS*, 267, 146
- Lynden-Bell, D., & Pringle, J. E. 1974, *MNRAS*, 168, 603
- Manara, C. F., Testi, L., Rigliaco, E., et al. 2013, *A&A*, 551, A107
- Marleau, G. D., Aoyama, Y., Kuiper, R., et al. 2022, *A&A*, 657, A38
- Matt, S., Goodson, A. P., Winglee, R. M., & Böhm, K.-H. 2002, *ApJ*, 574, 232
- Matt, S., & Pudritz, R. E. 2005, *ApJL*, 632, L135
- Mestel, L. 1961, *MNRAS*, 122, 473
- Miller, K. A., & Stone, J. M. 1997, *ApJ*, 489, 890
- Mishra, B., Begelman, M. C., Armitage, P. J., & Simon, J. B. 2020, *MNRAS*, 492, 1855
- Muzerolle, J., Calvet, N., & Hartmann, L. 2001, *ApJ*, 550, 944
- Muzerolle, J., Hartmann, L., & Calvet, N. 1998, *AJ*, 116, 455
- Narayan, R., Igumenshchev, I. V., & Abramowicz, M. A. 2003, *PASJ*, 55, L69
- Natta, A., Testi, L., Alcalá, J. M., et al. 2014, *A&A*, 569, A5
- Nelson, R. P., Gressel, O., & Umurhan, O. M. 2013, *MNRAS*, 435, 2610
- Newcomb, W. A. 1961, *Physics of Fluids*, 4, 391
- Porth, O., Mizuno, Y., Younsi, Z., & Fromm, C. M. 2021, *MNRAS*, 502, 2023
- Pringle, J. E., & Rees, M. J. 1972, *A&A*, 21, 1
- Proga, D., & Zhang, B. 2006, *MNRAS*, 370, L61
- Rein, H. 2012, *MNRAS*, 422, 3611
- Rigliaco, E., Natta, A., Testi, L., et al. 2012, *A&A*, 548, A56
- Rigliaco, E., Pascucci, I., Gorti, U., Edwards, S., & Hollenbach, D. 2013, *ApJ*, 772, 60
- Romanova, M. M., Blinova, A. A., Ustyugova, G. V., Koldoba, A. V., & Lovelace, R. V. E. 2018, *NewA*, 62, 94
- Romanova, M. M., Koldoba, A. V., Ustyugova, G. V., et al. 2020, *arXiv e-prints*, arXiv:2012.10826
- Romanova, M. M., Kulkarni, A. K., & Lovelace, R. V. E. 2008, *ApJL*, 673, L171
- Romanova, M. M., & Owocki, S. P. 2015, *SSRv*, 191, 339



- Romanova, M. M., Toropina, O. D., Toropin, Y. M., & Lovelace, R. V. E. 2003a, *ApJ*, 588, 400
- Romanova, M. M., Ustyugova, G. V., Koldoba, A. V., & Lovelace, R. V. E. 2004a, *ApJL*, 616, L151
- . 2004b, *ApJ*, 610, 920
- . 2011, *MNRAS*, 416, 416
- . 2012, *MNRAS*, 421, 63
- Romanova, M. M., Ustyugova, G. V., Koldoba, A. V., Wick, J. V., & Lovelace, R. V. E. 2003b, *ApJ*, 595, 1009
- Russo M., Thompson C., 2015, *ApJ*, 813, 81.
- Sauty, C., & Tsinganos, K. 1994, *A&A*, 287, 893
- Shakura, N. I., & Sunyaev, R. A. 1973, *A&A*, 24, 337
- Shu, F., Najita, J., Ostriker, E., et al. 1994, *ApJ*, 429, 781
- Spruit, H. C., Stehle, R., & Papaloizou, J. C. B. 1995, *MNRAS*, 275, 1223
- Stone, J. M., & Gardiner, T. 2007, *Physics of Fluids*, 19, 094104
- Stone, J. M., Gardiner, T. A., Teuben, P., Hawley, J. F., & Simon, J. B. 2008, *ApJS*, 178, 137
- Stone, J. M., Tomida, K., White, C. J., & Felker, K. G. 2020, *ApJS*, 249, 4
- Szulágyi, J., & Ercolano, B. 2020, *ApJ*, 902, 126
- Takasao, S., Tomida, K., Iwasaki, K., & Suzuki, T. K. 2018, *ApJ*, 857, 4
- . 2019, *ApJL*, 878, L10
- . 2022, *ApJ*, 941, 73
- Tchekhovskoy, A., Narayan, R., & McKinney, J. C. 2011, *MNRAS*, 418, L79
- Thanathibodee, T., Calvet, N., Bae, J., Muzerolle, J., & Hernández, R. F. 2019a, *ApJ*, 885, 94
- Thanathibodee, T., Calvet, N., Muzerolle, J., et al. 2019b, *ApJ*, 884, 86
- Thanathibodee, T., Molina, B., Serna, J., et al. 2023, *ApJ*, 944, 90
- Turner, N. J., Fromang, S., Gammie, C., et al. 2014, *Protostars and Planets VI*, 411
- Uzdensky, D. A., Königl, A., & Litwin, C. 2002, *ApJ*, 565, 1191
- van der Klis, M. 2006, in *Compact stellar X-ray sources*, Vol. 39, 39–112
- Wagner, K., Follete, K. B., Close, L. M., et al. 2018, *ApJL*, 863, L8
- Wang, Y., Zhu, Z., & Lin, D. N. C. 2023, arXiv e-prints, arXiv:2308.09129
- Wardle, M., & Königl, A. 1993, *ApJ*, 410, 218
- Weber, E. J., & Davis, Jr., L. 1967, *ApJ*, 148, 217
- Zanni, C., & Ferreira, J. 2013, *A&A*, 550, A99
- Zhou, Y., Bowler, B. P., Wagner, K. R., et al. 2021, *AJ*, 161, 244
- Zhu, Z. 2015, *ApJ*, 799, 16
- Zhu, Z., Dong, R., Stone, J. M., & Rafikov, R. R. 2015, *ApJ*, 813, 88
- Zhu, Z., & Stone, J. M. 2018, *ApJ*, 857, 34
- Zhu, Z., Stone, J. M., & Rafikov, R. R. 2013, *ApJ*, 768, 143

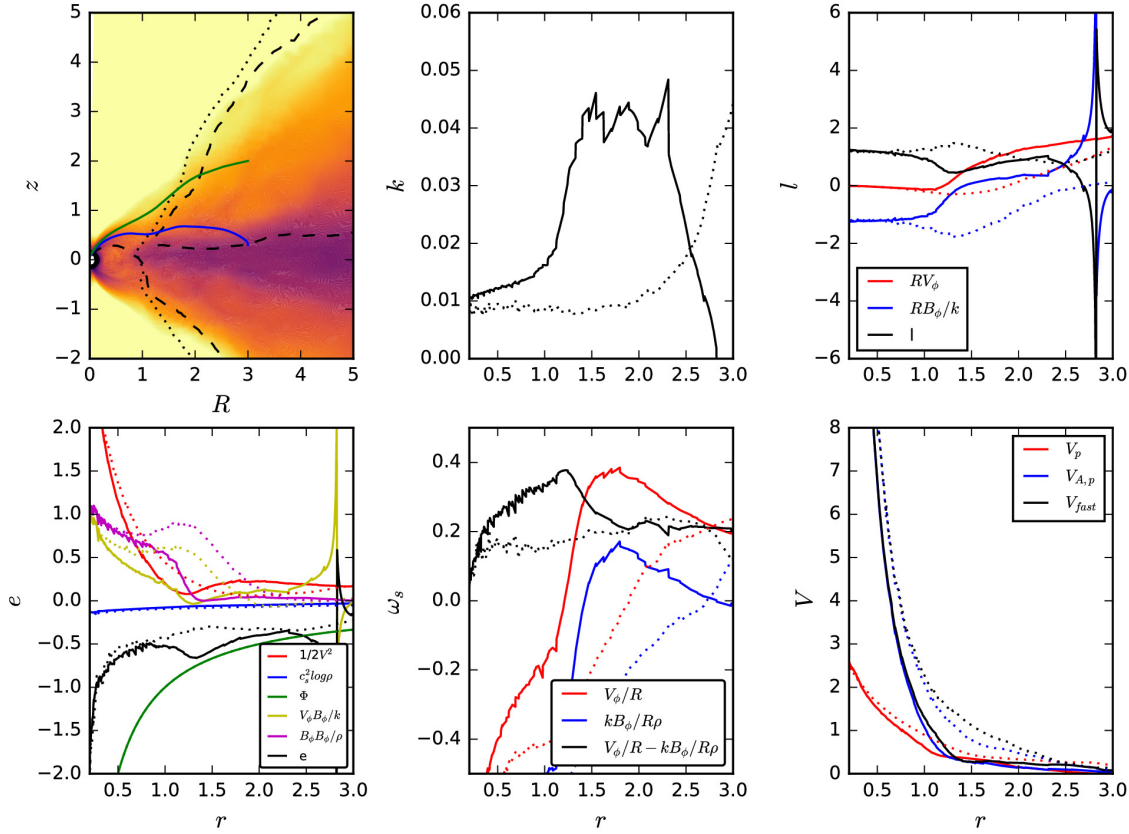


**Figure 25.** Various conserved quantities ( $k$ ,  $l$ ,  $e$ ,  $\omega$ ) and characteristic speeds (poloidal speed, Alfvén speed using polar B fields, and fast magnetosonic speed) along two fluid streamlines shown as the blue and green curves in the upper left panel. The dotted and dashed curves in the upper left panel represent where  $E_k = E_B$  and  $B_\phi = 0$ . The solid curves in the rest panels show quantities for the streamline starting at  $R=3$  and  $z = 0.3$ , while the dotted curves are for the streamline starting at  $R = 3$  and  $z = 2$ . All the primitive variables have been averaged over both the azimuthal direction and time (using 20 snapshots from  $t=66.2$  to  $68.2 T_0$ ). The streamlines are also calculated with the averaged velocity.

## APPENDIX

### A. CONSERVED QUANTITIES WITHIN THE MAGNETOSPHERE

Within the magnetosphere, magnetic fields are dominated by large-scale smooth fields ( $\langle B \rangle^2 / \langle B^2 \rangle \sim 1$  in the  $\langle B \rangle^2 / \langle B^2 \rangle$  panel of Figure 7). Although the flow is filamentary, the flow's azimuthally averaged properties may still follow the four conserved quantities ( $k$ ,  $l$ ,  $\omega_s$ ,  $e$ , Equations 1 to 4), which are plotted at the  $R - z$  plane in Figure 7 and along two streamlines in Figure 25. Figure 25 shows that the conserved quantities are roughly constant along fluid streamlines in the magnetically dominated region. The black solid and dotted curves in the  $k$ ,  $l$ ,  $\omega_s$ , and  $e$  panels show the four quantities along the blue and green curves in the upper left panel, and these quantities approach constant values within  $r \sim 1$  and  $2$  respectively. For these streamlines,  $r \sim 1$  and  $2$  coincide with the  $E_k = E_B$  boundary. The  $k$  value decreases significantly when the streamline is moving from the disc region to the magnetosphere region. This is also demonstrated in the  $k$  panel of Figure 7 where the  $E_k > E_B$  region has a higher  $k$  value. This higher mass loading factor for each streamline is related to the turbulent magnetic fields (or the break of the 2-D assumption) as shown in the  $\langle B \rangle^2 / \langle B^2 \rangle$  panel of Figure 7. The  $k$ ,  $\omega_s$  and  $l$  panels in Figure 7 all show sharp changes of values at the region where  $\langle B \rangle^2 / \langle B^2 \rangle$  suddenly becomes small. Different components of the conserved quantities are also shown in Figure 25. For  $l$ , we can see that the azimuthal magnetic fields dominate over angular momentum transport within the magnetosphere. For  $e$  at small  $r$ , the two dominant terms are the potential term and the kinetic energy term, which confirms the statement after Equation 4 that the inflow should have free-fall speed. For the black dotted curve,  $\omega_s$  is  $\sim 0.2$  before it drops towards zero within  $r \sim 0.5$ . Finally, the lower right panel of Figure 25 shows that the region having conserved quantities are sub-Alfvénic. The flow becomes sub-Alfvénic inside  $r \sim 1.3$  and  $2.5$  for these two streamlines, again corresponding to where  $E_k \sim E_B$ . We note that the conserved quantities are not strictly

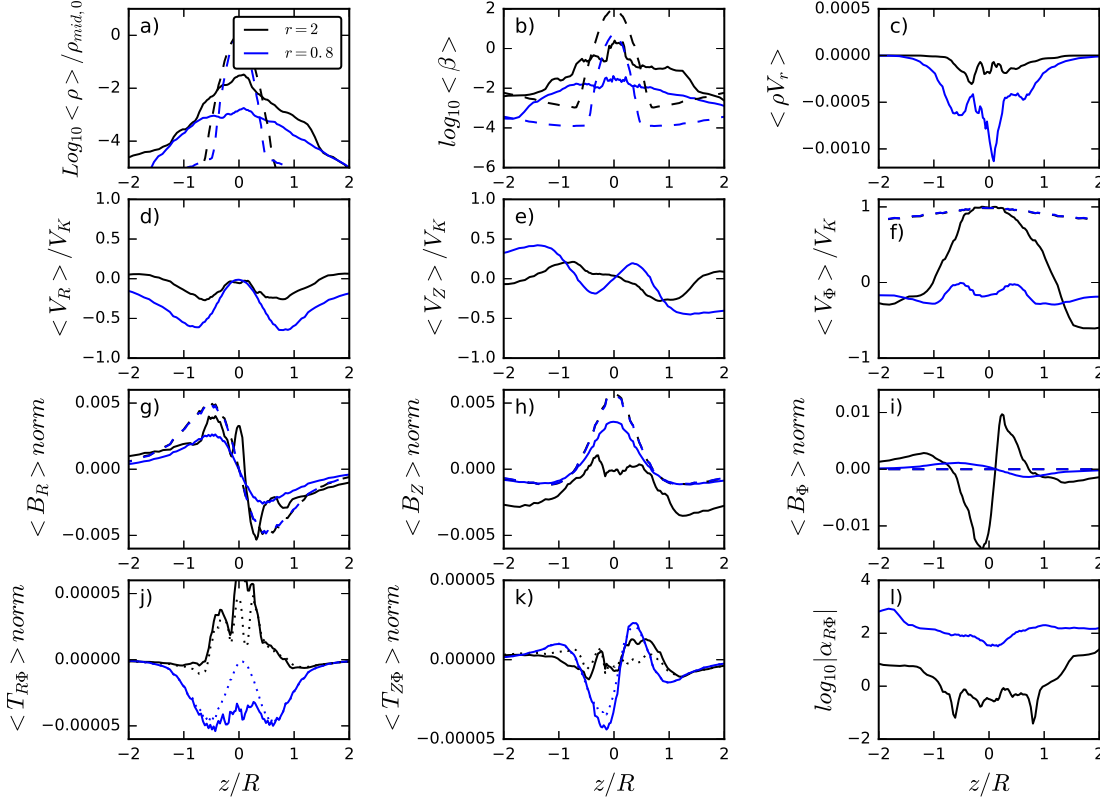


**Figure 26.** Various quantities along the vertical direction at  $R=0.8$  and  $2$ . All quantities are averaged over both the azimuthal direction and time (20 snapshots from  $66.2$  and  $68.2 T_0$ ). The dashed curves represent the initial condition. In the bottom two rows, the quantities at  $R = 0.8$  are multiplied by  $(0.8/2)^{-3}$  to compare with the quantities at  $R = 2$ . With this normalization, the initial magnetic fields at these two radii share the same profiles. The dotted curves in the  $\langle T_{R\phi} \rangle$  and  $\langle T_{Z\phi} \rangle$  panels are calculated with the space and time averaged velocities and magnetic fields. For the Reynolds stress component, the azimuthally averaged  $v_\phi$  has been subtracted.

constant within the magnetically dominated regions, especially for  $e$  and  $\omega_s$  along the streamline starting at  $R = 3$  and  $z=0.3$ . This is probably due to the turbulent structure. On the other hand, considering that the conserved quantities only vary by a factor of 2-3 while some components of the conserved quantities vary by one order of magnitude in the magnetically dominated region, we consider that the traditional 2-D axisymmetric steady-state model roughly captures the azimuthally-averaged flow structure inside the magnetic-dominated region. However, this only reflects some conversion between various components (e.g. the magnetic, motion, gravity components), and blindly extending the 2-D theory to describe the averaged 3-D flow structure can be misleading. With properly azimuthally averaging the fluid and induction equations, a better set of conserved quantities may be possible to describe the averaged flow, which is beyond the scope of this work.

## B. DISC STRUCTURE AND ANGULAR MOMENTUM TRANSPORT

To examine the disc structure in more detail, Figure 26 shows the profiles of various quantities along the  $z$  direction at  $R = 0.8$  and  $2$ . Since the magnetosphere is within  $R \sim 1$ , the profiles at  $R = 0.8$  and  $2$  respectively represent the magnetosphere and disc structure. With stronger magnetic fields, the density drops more at the inner radii. But the stronger magnetic fields also push the material to higher elevations. Compared with the initial condition, the density profile has a smoother transition from the midplane to the surface (Panel a of Figure 26). While the magnetosphere and the disc surface are magnetically dominated ( $\langle \beta \rangle \sim 10^{-4} - 10^{-1}$ ), the disc midplane is still matter dominated (Panel b). Within the magnetosphere, the radial velocity is approaching the Keplerian speed (also the free-fall speed). Within the disc surface region, the radial speed becomes supersonic at  $z \sim R$  (Panel d, with  $c_s \sim 0.1 v_k$ ). Since the disc density decreases towards a higher  $z$ , the mass flux rate at  $R = 2$  peaks at  $z \sim 0.3R$  or  $3H$  (Panel c). The azimuthal velocity becomes negative within the magnetosphere, while the disc midplane is still rotationally supported (Panel f). The poloidal magnetic fields still maintain the dipole configuration within both the magnetosphere and the disc region (Panel g and h). However, azimuthal fields are significantly amplified in the disc region (esp. at the disc surface), and



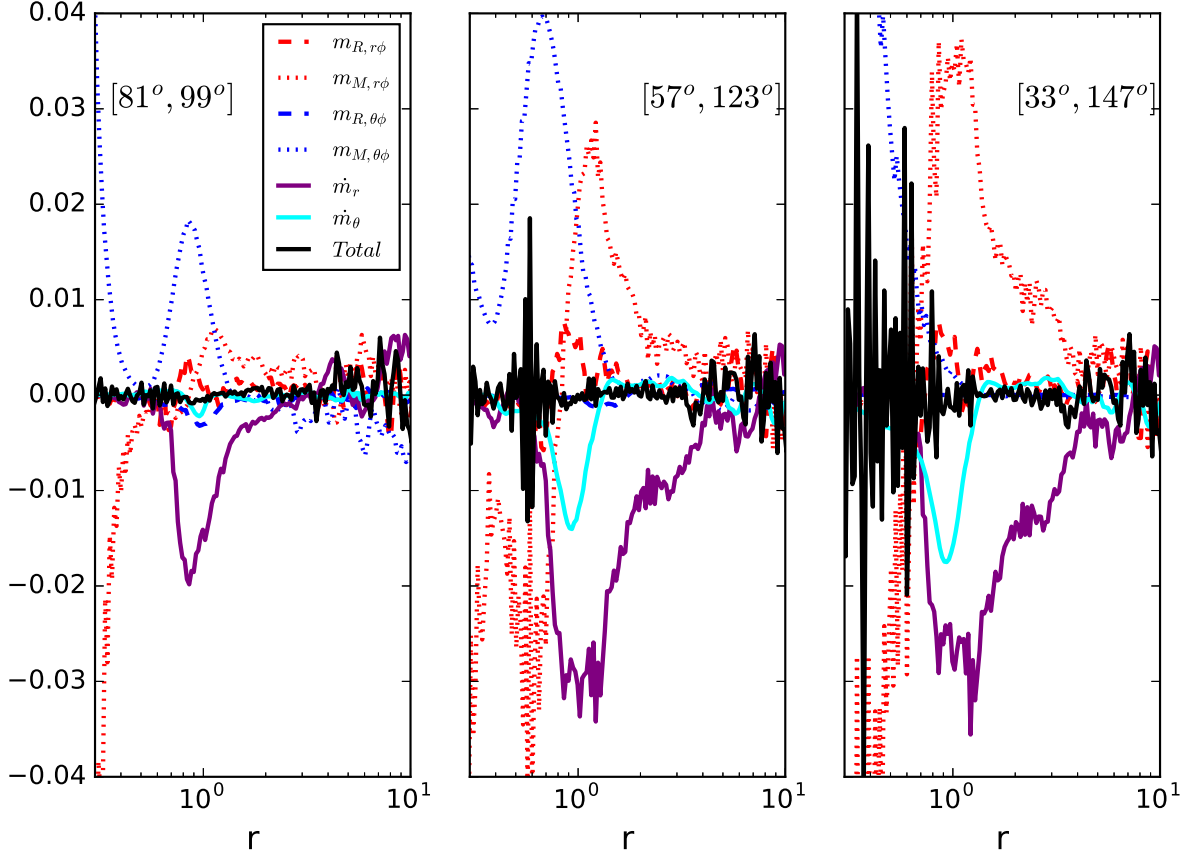


**Figure 27.** Various torque terms in Equation B3 integrated over different  $\theta$  limits (around disc midplane, surface accretion boundary, outflow boundary, from the left to right panels).

they can be several times stronger than the poloidal components (Panel i). Since  $B_\phi$  reverses its direction within the magnetosphere,  $\langle T_{R\phi} \rangle$  also changes the sign between the magnetosphere and the disc region (Panel j). While  $T_{z\phi}$  is comparable to  $T_{R\phi}$  within the magnetosphere at  $R = 0.8$ ,  $T_{z\phi}$  is much weaker than  $T_{R\phi}$  at the disc region ( $R = 2$ ) since  $B_z$  is much smaller than  $B_R$  there. Thus, most of angular momentum transport in the disc region, including both the midplane and the surface region, is still through  $T_{R\phi}$ . The  $T_{R\phi}$  stress mostly comes from the turbulent stress at the midplane, while it is from the net fields at the surface accretion region ( $z/R \sim 1$ ) (by comparing dotted and solid curves in Panel j).

To understand the roles played by  $r$ - $\phi$  and  $\theta$ - $\phi$  stress terms, we write the angular momentum conservation equation in a spherical-polar coordinate system:

$$\begin{aligned} \frac{\partial \langle r \sin \theta \rho \delta v_\phi \rangle}{\partial t} &= -\frac{\sin \theta}{r^2} \frac{\partial (r^3 \langle \rho v_r \delta v_\phi - B_r B_\phi \rangle)}{\partial r} - \sin \theta \langle \rho v_r \rangle \frac{\partial r \bar{v}_\phi}{\partial r} \\ &\quad - \frac{1}{\sin \theta} \frac{\partial (\sin^2 \theta \langle \rho v_\theta \delta v_\phi - B_\theta B_\phi \rangle)}{\partial \theta} - \langle \rho v_\theta \rangle \frac{\partial (\sin \theta \bar{v}_\phi)}{\partial \theta} \end{aligned} \quad (\text{B1})$$

where  $\delta v_\phi = v_\phi - \bar{v}_\phi$  and  $\bar{v}_\phi$  is the azimuthally averaged  $v_\phi$ . If we integrate the equation over the poloidal and azimuthal directions weighted by area ( $r^2 \sin \theta$ ), we have

$$\begin{aligned} \frac{\partial \int r^3 \sin^2 \theta \langle \rho \delta v_\phi \rangle d\theta}{\partial t} &= - \int \sin^2 \theta \frac{\partial (r^3 \langle \rho v_r \delta v_\phi - B_r B_\phi \rangle)}{\partial r} d\theta - \int r^2 \sin^2 \theta \langle \rho v_r \rangle \frac{\partial r \bar{v}_\phi}{\partial r} d\theta \\ &\quad - \int r^2 \frac{\partial (\sin^2 \theta \langle \rho v_\theta \delta v_\phi - B_\theta B_\phi \rangle)}{\partial \theta} d\theta - \int r^2 \sin \theta \langle \rho v_\theta \rangle \frac{\partial (\sin \theta \bar{v}_\phi)}{\partial \theta} d\theta \end{aligned} \quad (\text{B2})$$

or simply

$$\frac{\partial \int r^3 \sin^2 \theta \langle \rho \delta v_\phi \rangle d\theta}{\partial t} = -m_{R,r\phi} - m_{M,r\phi} - \dot{m}_r - m_{R,\theta\phi} - m_{M,\theta\phi} - \dot{m}_\theta. \quad (\text{B3})$$

The left term is the change of angular momentum. In a quasi-steady state, it is zero. The first two terms on the right side of Equation B3 are the radial gradients of the Reynolds and Maxwell  $r$ - $\phi$  stresses. The stresses could be due to MRI turbulence (e.g. at the disc midplane) or large-scale organized magnetic fields (e.g. at the disc surface). The third term on the right is the radial advection term which represents angular momentum carried by the radial accretion flow. The last three terms on the right are similar to the first three terms except that they describe  $\theta$ - $\phi$  stresses and advection in the  $\theta$  direction (e.g. flow in the  $\theta$  direction).

We calculate these terms from our simulation by averaging 310 snapshots from 65.1 to 68.2  $T_0$ . We integrate these terms over the  $\theta$  direction for different sized wedges, shown in Figure 27. We can see that the disc has reached a quasi-steady state within  $R \sim 6$ , where the black curves have much smaller values than other curves. The plots also show that the Maxwell stress (dotted curves) dominates over the Reynolds stress (dashed curves). Within 1.5 disc scale heights above and below the midplane (the leftmost panel), the disc is matter dominated ( $\langle\beta\rangle \gtrsim 1$ ) beyond  $R \sim 1.5$ . The radial mass flux is quite low at this region around the midplane. Instead of driving the radial inflow (the  $\dot{m}_r$  term), the  $r$ - $\phi$  stress is balanced by the  $\theta$ - $\phi$  stress at  $R \gtrsim 2$ . Thus, the magnetic breaking from the midplane to the surface transports angular momentum into the midplane, which reduces the midplane’s radial inflow. Only within the magnetically supported surface region at  $r \lesssim 1.5$ , the  $\theta$ - $\phi$  stress removes the flow’s angular momentum, leading to disc accretion. Within the highly magnetized region ( $r \lesssim 0.6$ ), the  $r$ - $\phi$  and  $\theta$ - $\phi$  magnetic stresses balance each other again, indicating that magnetic fields there follow the force-free solution. If we include the disc surface in the integration (middle and right panels), we can see that the radial inflow now becomes significant beyond  $R \sim 1.5$  and is mainly driven by the  $r$ - $\phi$  stress. The advection in the  $\theta$  direction also carries part of angular momentum away, but it is much smaller than the  $r$ - $\phi$  stress, except around the magnetosphere boundary at  $r \sim 1$ . The  $\theta$ - $\phi$  stress is also much weaker than the  $r$ - $\phi$  stress in the disc region. It only becomes important within the magnetosphere. Overall, in the disc region beyond the magnetosphere, the flow and magnetic structure are very similar to the net vertical field simulations in Zhu & Stone (2018), with the  $r$ - $\phi$  stress leading to the overall radial inflow and the  $\theta$ - $\phi$  stress connecting the surface to the midplane.

On the other hand, there are significant differences between this simulation and that in Zhu & Stone (2018), mainly due to the dipole field configuration. Very high above the disc surface ( $z \gtrsim R$ ), magnetic fields are pointing down towards the central star ( $\langle B_\phi \rangle$  panels in Figure 12).  $B_\phi$  there thus becomes negative due to the differential motion between the non-rotating star and the Keplerian disc. Material that follows the field lines moving inwards have negative  $v_\phi$ , as explained in §2.1. For the net vertical field simulations, the fields at  $z \gtrsim R$  are pointing upwards. The anchor points at  $z \sim R$  drag the field lines in the direction of disc rotation. This generates negative  $B_\phi$  and launches disc wind like “beads on the wire” (Blandford & Payne 1982). At  $B_\phi = 0$ , which is close to the wind launching point, the flow’s azimuthal angular frequency  $\Omega$  equals the conserved constant  $\omega_s$  (Equation 2). When the wind is moving outwards along the field lines,  $\Omega$  decreases as  $B_\phi$  becomes more negative. However, this decrease of  $\Omega$  is slower than the decrease of the Keplerian frequency with  $R$  ( $R^{-3/2}$ ), so that the wind flow appears to be super-Keplerian compared with the local flow at  $R$  (the  $v_\phi$  panel in the bottom row of Figure 12). Overall, for the material high above the disc surface, the flow has opposite  $r$  and  $\phi$  directions between the magnetospheric accretion disc and the disc with net vertical fields.